RESSALVA

Atendendo solicitação do(a) autor(a), o texto completo desta tese será disponibilizado somente a partir de 29/05/2024.

Lanthanide-based upconverting and chromium-based persistent luminescence nanoparticles for optical applications involving NIR illumination

Ph.D. thesis

York Estewin Serge Correales

Universidade Estadual Paulista
Campus de Araraquara
Programa De Pós-Graduação Em Química

Araraquara
2022

YORK ESTEWIN SERGE CORREALES

Lanthanide-based upconverting and chromium-based persistent luminescence nanoparticles for optical applications involving NIR illumination

Thesis presented to the Institute of Chemistry, São Paulo State University, to obtain the Ph.D in Chemistry

Advisor: Prof. Dr. Sidney José Lima Ribeiro
Co- Advisor: Prof. Dr. Sajjad Ullah

Araraquara
2022

YORK ESTEWIN SERGE CORREALES

Nanopartículas de conversão ascendente de energia baseadas em lantanídeos e de luminescência persistente baseadas em crômio para aplicações ópticas envolvendo radiação no infravermelho próximo

Tese apresentada ao Instituto de Química, Universidade Estadual Paulista, como parte dos requisitos para obtenção do título de Doutor em Química.

Orientador: Prof. Dr. Sidney José Lima Ribeiro
Coorientador: Prof. Dr. Sajjad Ullah

Araraquara
2022

C824l

Correales, York Estewin Serge

Lanthanide-based upconverting and chromium-based persistent luminescence nanoparticles for optical applications involving NIR illumination / York Estewin Serge Correales. -- Araraquara, 2022

226 f. : il., tabs.

Thesis (doctor) - Universidade Estadual Paulista (Unesp), Instituto de Química, Araraquara

Advisor: Sidney José Lima Ribeiro

Co-advisor: Sajjad Ullah

1. Inorganic chemistry. 2. Rare earth metals. 3. Nanoparticles. 4. Luminescence. 5. Photocatalysis. I. Título.

Sistema de geração automática de fichas catalográficas da Unesp. Biblioteca do Instituto de Química, Araraquara. Dados fornecidos pelo autor(a).

Essa ficha não pode ser modificada.

CERTIFICADO DE APROVAÇÃO

TÍTULO DA TESE: "Nanopartículas de conversão ascendente de energia baseadas em lantanídeos e de luminescência persistente baseadas em crômio para aplicações ópticas envolvendo radiação no infravermelho próximo".

AUTOR: YORK ESTEWIN SERGE CORREALES
ORIENTADOR: SIDNEY JOSE LIMA RIBEIRO
COORIENTADOR: SAJJAD ULLAH

Aprovado como parte das exigências para obtenção do Título de , pela Comissão Examinadora:

Sidney Jose Lima Ribeiro:01830169807
Assinado de forma digital por Sidney Jose Lima Ribeiro:01830169807
Dados: 2022.11.30 15:32:29 -03'00'

Prof. Dr. SIDNEY JOSE LIMA RIBEIRO (Participaçao Virtual)
Departamento de Quimica Analitica, Fisico-Quimica e Inorganica / Instituto de Quimica - UNESP - Araraquara

Prof. Dr. YOUNES MESSADDEQ (Participaçao Virtual)
Departamento de Química Analítica, Físico-Química e Inorgânica / Instituto de Química - UNESP - Araraquara

Prof. Dr. LUCIANA REYES PIRES KASSAB (Participaçao Virtual)
Laboratório de Tecnologia em Materiais Fotônicos e Optoeletrônicos / Faculdade de Tecnologia de São Paulo - FATEC - São Paulo

Prof. Dr. LUCAS CARVALHO VELOSO RODRIGUES (Participaçao Virtual)
Departamento de Química Fundamental / Instituto de Química - USP - São Paulo

Prof. Dr. DOUGLAS FAZA FRANCO (Participaçao Virtual)
Departamento de Química Analítica, Físico-Química e Inorgânica / Instituto de Química - UNESP - Araraquara

Araraquara, 29 de novembro de 2022

I definitely dedicate this and each one of my achievements to my parents Cesar and Alba, my brothers Cesar and Keybis, and my darling wife Nayara. I admire them and they are my main source of inspiration.

ACKNOWLEGMENT

From the moment I left my country to start this doctorate, I knew that it would be an experience that would change my life. And yes, great important changes on a personal and professional level occurred, which would not have been possible without the support, advice and guidance that I received from many people throughout these years.

First, my deep gratitude to God for the life, for holding me strong, and for the people he has placed in my path.

I am pleased to have been supervised by Prof. Dr. Sidney Ribeiro, whom I sincerely thank for the trust he has placed in me, his constant advice and his valuable leadership.

I am very grateful to my co-supervisor, Sajjad Ullah, for everything he has done for me. His advice and guidance, as well as his brotherhood have been of great influence in my professional and scientific development.

I would like to thank Prof. Marc Verelst, his entire team, and the CEMES - CNRs in Toulouse - France, for the opportunity, support, and hospitality during my research internship abroad.

I am extremely grateful to the Institute of Chemistry of the São Paulo State University and to all the professors who directly or indirectly had an impact on my PhD studies.

I sincerely appreciate all my lab-mates and professors of the Laboratory of Photonic Materials in Araraquara. I am very pleased to have shared moments, experiences, and knowledge with each of them. Their valuable comments and suggestions on my studies, reports, presentations, and publications encouraged me to try harder.

I would like to express my sincere gratitude to Rafael Domeneguetti for his entire willingness to help and his friendship.

I thank all the co-authors of the published, accepted and/or in-progress works for their collaboration and partnership, especially Chanchal Hazra from whom I learned a lot. I would also like to thank all those colleagues who gave me the opportunity to take part in their research as a collaborator.

My most sincere and deepest appreciations go to my wife, Nayara de Melo Costa Serge, for her unconditional and constant support, as well as for motivating me every

day to be better and work harder. The words of thanks that I can write here may not be enough to express how grateful I am to her.

From the bottom of my heart, I thank my family for their great encouragement and unstoppable support over the years. They are always my biggest inspiration.

I especially thank my aunt Edelmira, who left early, but who I feel with me, taking care of me every day. I am eternally grateful for the time we spent together while she was here.

I also express my sincere gratitude to all my childhood and school friends -friend for life- for every experience lived together and for every word of support.

I would like to thank the financial support from the Brazilian agencies: Fundação de Amparo à Ciência e Tecnologia do Estado de São Paulo (FAPESP) for the grants No. 2018/15791-7 and 2020/09339-4, Conselho Nacional de Desenvolvimento Científico e Tecnológico for the grant No. 133105/2017-2, and Coordenação de Aperfeiçoamento de Pessoal de Nível Superior (CAPES) for all financing -code 001.

I also thank Nanoscale Advances The Royal Chemistry Society, Materials Advances The Royal Chemistry Society, and Langmuir American Chemical Society for their kind permission to reproduce and use the content of published/accepted articles in this thesis.

DATA

Personal Information

Full name: York Estewin Serge Correales

Name in bibliography citation: Y. E. Serge-Correales, Serge, Y.; Serge, York; Serge-Correales, Y. E.; York E. Serge C.

Nationality: Colombian

Birth city: Barranquilla, Atlántico, Colombia

Profession: Chemist

Address: Instituto de Química - Universidade Estadual Paulista “Júlio de Mesquita Filho” - Av. Prof. Francisco Degni, 55 - Jardim Quitandinha – Araraquara – SP

CEP: 14800-060

e-mail: yorkestewin@gmail.com

Academic education

Bachelor's degree in Chemistry (2016), Universidad del Atlántico, Barranquilla – Colombia.

Work Experience

Internship (07/2014-01/2015) - TRIPLE A, Barranquilla – Colombia

Quality Control Laboratory Analyst (08/2016 to 02/2017) – QUIMICA INTERNACIONAL S A, Barranquilla – Colombia

Student research internship (01/12/2020 to 30/11/2021) – CENTRE D'ELABORATION DE MATERIAUX ET D'ETUDES STRUCTURALES, Toulouse – France

Hosted trainee (06/02/2022 to 12/03/2022) – CENTRE D'ELABORATION DE MATERIAUX ET D'ETUDES STRUCTURALES, Toulouse – France

Participation in scientific events

- XIX Brazil MRS Meeting (Sep 25 – 29, 2022, Foz do Iguaçu - Pr – Brasil). Synthesis, surface modification, and functionalization of $ZnGa_2O_4:Cr^{3+}$ persistent luminescence nanoparticles for biosensing (poster presentation).
- XXX International Materials Research Congress and International Conference on Advanced Materials (Aug 14 – 19, 2022, Cancun, Mexico). A UV-visible-NIR active photocatalytic system based on $NaYbF_4:Tm^{3+}/Ag_3PO_4/H_2O_2$ for broad spectrum photocatalysis (oral presentation)
- XIX Brazil MRS Meeting (Aug 30 – Sep 03, 2021, online format). Photocatalytic system based on upconverting particles/photocatalyst/oxidant Thulium-doped sodium ytterbium fluoride/silver phosphate/hydrogen peroxide activated under visible and near infrared light (poster presentation).
- 42ª Reunião Anual da Sociedade Brasileira de Química (May 27 - 30, 2019, Joinville - SC - Brasil). Multicolor Emission through Bi-directional Energy Transfer in Nd^{3+}-Sensitized Gd^{3+}-based Core/Shell/Shell Upconverting Nanoparticles (oral and poster presentation).
- 8th International Conference on Optical, Optoelectronic and Photonic Materials and Applications (Aug 26 - 31, 2018, Maresias – SP - Brasil). Nd^{3+}-Sensitized Gd^{3+}-based Core/Shell/Shell Upconverting Nanoparticles: A Platform for Multicolour Emissions through Bi-directional Energy Transfer (poster presentation).
- 10th International Conference on Nanophotonics (Jul 02 - 05, 2017, Recife-Pe-Brasil) Size-controlled synthesis of Nd^{3+}-sensitized Core@shell Upconversion Particles (poster presentation).
- XI Encuentro Departamental de Semilleros de Investigación (May 16 - 17, 2014, Barranquilla - Colombia. Evaluación del Carácter Generador de Oxígeno Singulete por Derivados Pirido[2,3-d]Pirimidínicos (oral presentation).
- X Encuentro Departamental de Semilleros de Investigación (May 29 - 31, 2013, Barranquilla - Colombia. Determinación del Rendimiento Cuántico de Producción de Oxígeno Singulete de 7-Indolilpirido[2,3-d]Pirimidinas (oral presentation.

Scientific Productions

- **Y.E. Serge-Correales**, D. Neumeyer, S. Ullah, R. Mauricot, Q. Zou, S.J.L. Ribeiro, M. Verelst, Size control and improved aqueous colloidal stability of surface-functionalized $ZnGa_2O_4:Cr^{3+}$ bright persistent luminescence nanoparticles. *Langmuir*. Accepted manuscript. Doi: 10.1021/acs.langmuir.2c02871
- J. Galindo, A. Pessoa, **Y.E. Serge-Correales**, S.J.L. Ribeiro, L. de S. Menezes, A. Amarala, Method for separating overlapping multiphoton upconverted emission bands through spectral power dependence analysis. J. Lumin. Accepted manuscript. Doi: https://doi.org/10.1016/j.jlumin.2023.119685
- A. Pessoa, J. Galindo, **Y.E. Serge-Correales**, A. Amaral, S.J.L. Ribeiro, L. Menezes, 2D thermal maps using hyperspectral scanning of single upconverting microcrystals: experimental artifacts and image processing. *ACS Appl. Mater. Interfaces* **2022**, 14, 38311–38319.
- **Y.E Serge-Correales**, S. Ullah, E. P. Ferreira-Neto, H. D. Rojas-Mantilla, C. Hazra, S.J.L. Ribeiro, A UV-visible-NIR active smart photocatalytic system based on $NaYbF_4:Tm^{3+}$ upconverting particles and Ag_3PO_4/H_2O_2 for photocatalytic processes under light on/light off conditions. *Mater. Adv.* **2022,** 3, 2706–2715.
- I. M. Gonçalves, A. Pessoa, C. Hazra, **Y.E Serge-Correales**, S.J. Ribeiro, L. de S. Menezes, Phonon-assisted NIR-to-visible upconversion in single β-$NaYF_4$ microcrystals codoped with Er^{3+} and Yb^{3+} for microthermometry applications: Experiment and theory. *J. Lumin.* **2021**, 231, 117801.
- S. Ullah, A.A. Khan, A. Jan, S.Q. Aain, E.P. Neto, **Y.E. Serge-Correales**, R. Parveen, H. Wender, U.P. Rodrigues-Filho, S.J. Ribeiro, Enhanced photoactivity of $BiVO_4/Ag/Ag_2O$ Z-scheme photocatalyst for efficient environmental remediation under natural sunlight and low-cost LED illumination. *Colloids Surf. A Physicochem. Eng. Asp.* **2020**, 600, 124946.
- **Y.E. Serge-Correales**, C. Hazra, S. Ullah, L. Roncalho, S.J.L. Ribeiro, Precisely Tailored *Shell* Thickness and Ln^{3+} Content to Produce Multicolor Emission from Nd^{3+}-Sensitized Gd^{3+}-Based *Core*/*Shell*/*Shell* UCNPs Through Bi-directional Energy Transfer, *Nanoscale Adv.* **2019**, 1, 1936–1947.

- S. Ullah, E.P. Ferreira-Neto, C. Hazra, R. Parveen, H.D. Rojas-Mantilla, M.L. Calegaro, **Y.E. Serge-Correales**; U.P. Rodrigues-Filho, S.J.L. Ribeiro, Broad spectrum photocatalytic system based on $BiVO_4$ and $NaYbF_4$:Tm^{3+} upconversion particles for environmental remediation under UV-vis-NIR illumination, *Appl. Catal. B Environ.* **2019**, 243, 121–135.
- C. Hazra, S. Ullah, **Y.E. Serge-Correales**, L.G. Caetano, S.J.L. Ribeiro, Enhanced NIR-I emission from water-dispersible NIR-II dye-sensitized core/active shell upconverting nanoparticles, *J. Mater. Chem. C* **2018**, 6, 4777–4785.
- J. Rangel, C.D. Uribe, A.R. Serrano, X. Zarated, **Y.E. Serge-Correales**, W. Vallejo, M. Nogueras, J. Trilleras, J. Quiroga, J. Tatchen, J. Cobo, Three-Component One-Pot Synthesis of Novel Pyrido[2,3-*d*]Pyrimidine Indole Substituted Derivatives and DFT Analysis. *J. Mol. Struct.* **2017**, 1137, 431–439.

FOREWORD

This thesis was written in the format of chapters/articles in accordance with the presentation of dissertations and theses norms of the Chemistry Graduate Program at the Institute of Chemistry, UNESP – Araraquara – SP.

The content of Chapter 3 is reproduced from a paper that was published in Nanoscale Advances after peer review. This is reproduced with the permission of all co-authors and Copyright 2019 The Royal Society of Chemistry. To access the final edited and published work see https://doi.org/10.1039/C9NA00006B

The content of Chapter 4 is reproduced from an article that was published in Materials Advances after peer review. This is reproduced with the permission of all co-authors and Copyright 2022 The Royal Society of Chemistry. To access the final edited and published work see https://doi.org/10.1039/D1MA01028J

The content of Chapter 5 is reproduced from a manuscript that was accepted for publication in Langmuir after peer review. This is reproduced with the permission of all co-authors and Copyright 2023 American Chemical Society. To access the final edited and published work see https://doi.org/10.1021/acs.langmuir.2c02871

The content of Chapter 6 has not yet been submitted to any journal because it is not fully completed.

The results corresponding to Chapters 3 and 4 were collected at the host institution. Meanwhile, most of the results corresponding to Chapters 5 and 6 were collected during the studies abroad at CEMES–CNRs in Toulouse–France, and a little part at the host institution. More detailed information about the manuscripts that make up this thesis is presented below.

Chapter 3 Precisely tailored shell thickness and Ln^{3+} content to produce multicolor emission from Nd^{3+}-sensitized Gd^{3+}-based core/shell/shell UCNPs through bi-directional energy transfer

Authors York E. Serge Correales, Chanchal Hazra, Sajjad Ullah, Laís R. Lima, and Sidney J. L. Ribeiro

Journal Nanoscale Adv., 2019, 1, 1936–1947.

DOI 10.1039/C9NA00006B

State Received on January 4, 2019; Accepted on March 20, 2019; First published on March 21, 2019.

Chapter 4 A UV-visible-NIR active smart photocatalytic system based on $NaYbF_4:Tm^{3+}$ upconverting particles and Ag_3PO_4/H_2O_2 for photocatalytic processes under light on/light off conditions

Authors York E. Serge-Correales, Sajjad Ullah, Elias P. Ferreira-Neto, Hernan D. Rojas-Mantilla, Chanchal Hazra, and Sidney J. L. Ribeiro

Journal Mater. Adv., 2022, 3, 2706–2715

DOI 10.1039/D1MA01028J

State Received on November 4, 2021; Accepted on December 24, 2021; First published on December 24, 2021.

Chapter 5 Size control and improved aqueous colloidal stability of surface-functionalized $ZnGa_2O_4:Cr^{3+}$ bright persistent luminescence nanoparticles

Authors York E. Serge-Correales, David Neumeyer, Sajjad Ullah, Robert Mauricot, Qilin Zou, Sidney J. L. Ribeiro, and Marc Verelst

Journal Langmuir

DOI 10.1021/acs.langmuir.2c02871

State Received on October 20, 2022; Accepted on January 3, 2023.

Chapter 6 Coupling of $NaYbF_4:Tm^{3+}$ upconverting nanoparticles with $ZnGa_2O_4:Cr^{3+}$ persistent luminescence nanoparticles

Authors York E. Serge-Correales, David Neumeyer, Sajjad Ullah, Robert Mauricot, Sidney J. L. Ribeiro, and Marc Verelst

Journal This work is expected to be submitted to ACS Applied Nano Materials upon completion.

ABSTRACT

This work reports the development of luminescent materials with upconversion (UC) and persistent luminescence (PL) properties for optical applications involving near-infrared (NIR) illumination. The following are described and discussed: 1) controlled synthesis to obtain uniform and monodisperse nano- and micro-particles; 2) surface modification to provide hydrophilic functional groups, making them dispersible and stable in aqueous media; 3) the structural, morphological, optical and photoluminescent characterizations; 4) potential applications.

Sub-20 nm core/multishell $NaGdF_4:Yb^{3+}/Ca^{2+}/Nd^{3+}/Tm^{3+}@NaGdF_4:Nd^{3+}/Ca^{2+}@NaGdF_4:Yb^{3+}/Ca^{2+}/Er^{3+}/Nd^{3+}$ UC nanoparticles (UCNPs) were obtained by seed-mediated growth *via* high-temperature co-precipitation route. Through simple and precise control of the shell thickness along with tuning the content of lanthanide ions in each domain (core, middle shell, and outermost shell) it was possible to obtain multicolored and tunable luminescence from blue to white under 808 nm laser excitation.

$NaYbF_4:Tm^{3+}$ UC particles (UCPs) with microrod shape of 8 μm in length and 2.5 μm in diameter were also synthesized. These microrods in conjunction with Ag_3PO_4 particles (photocatalyst) and H_2O_2 (oxidizing agent) were used in the development of a broad-spectrum photocatalytic system, active in the UV-Vis-NIR region. This photocatalytic system showed high photocatalytic activity in crystal violet (CV) dye degradation under both direct excitation with visible light (complete dye removal in less than 8 min) and indirect excitation of Ag_3PO_4 in the NIR due to photons emitted by the UCPs under 980 nm laser irradiation (almost total dye removal in approximately 90 min).

Furthermore, uniform OA-capped $NaYbF_4:Tm^{3+}@NaYF_4$ core/shell UCNPs were synthesized. The UC property of these nanoparticles was improved by increasing the protection of the $NaYbF_4:Tm^{3+}$ core nanoparticles with a $NaYF_4$ protective layer of different thickness. Increasing shell thickness led to a concomitant decrease in energy quenching associated with surface defects of the unprotected nanoparticles.

To enhance the applications of these $NaYbF_4:Tm^{3+}@NaYF_4$ UCNPs, their coupling with PL nanoparticles (PLNPs) was investigated, aiming at obtaining a system that presents UC and PL (UC-PL) with excitation and emission in the NIR, which may find

potential applications in deep tissue luminescence bioimaging or in the activation of photosensitizers in the photodynamic therapy.

As a result, OA-coated $ZnGa_2O_4:Cr^{3+}$ (ZGO) PLNPs were first synthesized. The synthesis was carried out by solvothermal treatment at 210 °C, without the need for further calcination. Tunable size from 7 to 21 nm was achieved using different alcohols in the synthesis and a seed-mediated nanoparticle growth approach. The PL was nanoparticle size-dependent (PL lasting over 1000 s).

After improving the optical properties of the OA-coated nanoparticles, the ligand exchange process for surface modification was carried out. This allowed removing hydrophobic ligands and anchoring hydrophilic groups provided by poly(acrylic acid) (PAA) polymer and cysteamine (Cys) molecules on the surface of the nanoparticles, ensuring their redispersion in aqueous media, as well as providing long-term colloidal stability.

Finally, the coupling reactions of hydrophilic nanoparticles were investigated through the formation of covalent bonds between surface-functionalized UCNPs and PLNPs, on the basis of EDC/NHS (1-ethyl-3-(-3-dimethylaminopropyl) carbodiimide hydrochloride)/(N-Hydroxysuccinimide) coupling chemistry. The results obtained suggest that the coupling reaction was successfully performed. However, new coupling conditions and characterizations are needed, as well as the study of the energy transfer between the nanoparticles for a better understanding of this coupling process and to guarantee future applications.

RESUMO

Neste trabalho é relatado o desenvolvimento de materiais luminescentes com propriedades de UC e PL envolvendo radiação no NIR. São descritas e discutidas: 1) a síntese controlada para a obtenção de nano e micropartículas monodispersas e de tamanho uniforme; 2) a modificação da superfície para fornecer grupos funcionais hidrofílicos, tornando-as dispersíveis e estáveis em meio aquoso; 3) caracterizações: estrutural, morfológica, óptica e fotoluminescente; 4) as potenciais aplicações.

UCNPs com tamanho menor que 20 nm, estrutura do tipo núcleo/multicamada e de composição/design representado como $NaGdF_4:Yb^{3+}/Ca^{2+}/Nd^{3+}/Tm^{3+}@NaGdF_4:Nd^{3+}/Ca^{2+}@NaGdF_4:Yb^{3+}/Ca^{2+}/Er^{3+}/Nd^{3+}$ foram obtidas por crescimento mediado por sementes através de uma rota de coprecipitação a 300 °C. Mediante o controle simples e preciso da espessura das diferentes camadas, juntamente com ajuste do conteúdo dos íons lantanídeos em cada domínio (núcleo, camada intermediária e camada mais externa) foi possível obter luminescência multicolorida e sintonizável do azul ao branco sob excitação laser de 808 nm.

Também foram sintetizadas UCPs de $NaYbF_4:Tm^{3+}$ em formato de microbastões de 8 µm de comprimento e 2,5 µm de diâmetro. Estes microbastões, juntamente com partículas de Ag_3PO_4 (fotocatalisador) e H_2O_2 (agente oxidante) foram utilizados no desenvolvimento de um sistema fotocatalítico de amplo espectro, ativo no UV-Vis-NIR. O sistema fotocatalítico desenvolvido apresentou alta atividade fotocatalítica na degradação do corante cristal violeta (CV) sob irradiação com luz visível (remoção total do corante em menos de 8 min) e no NIR usando um laser de 980 nm (quase total remoção do corante em aproximadamente 90 min).

Além disso, foram sintetizadas UCNPs de tamanho uniforme, de estrutura do tipo núcleo/casca e de composição/design representado como $NaYbF_4:Tm^{3+}@NaYF_4$. A propriedade de UC destas nanopartículas foi aprimorada mediante o aumento da proteção das nanopartículas centrais (núcleo) de $NaYbF_4:Tm^{3+}$ com uma camada protetora de $NaYF_4$ cada vez maior. O aumento da espessura da casca levou a uma diminuição concomitante da supressão da energia associada aos defeitos de superfície das nanopartículas sem revestimento.

Para potencializar as aplicações destas UCNPs de $NaYbF_4:Tm^{3+}@NaYF_4$ foi investigado seu acoplamento com nanopartículas de PL (PLNPs), visando a obtenção de um sistema que apresente UC e PL (UC-PL) com excitação e emissão no NIR, que

podem encontrar aplicações potenciais em bioimagem de tecido profundo baseado em luminescência ou na ativação de fotosensibilizadores na terapia fotodinâmica.

Em decorrência disso, primeiramente foram sintetizadas PLNPs de composição $ZnGa_2O_4:Cr^{3+}$ (ZGO) revestidas com OA. A síntese foi realizada pelo tratamento solvotérmico a 210 °C, sem a necessidade de calcinação adicional. Foi possível controlar o tamanho de 7 a 21 nm usando diferentes álcoois na síntese e uma abordagem de crescimento de nanopartículas mediada por sementes. A luminescência persistente foi dependente do tamanho das nanopartículas (PL com duração acima de 1000 s).

Após do aprimoramento das propriedades ópticas das nanopartículas revestidas com OA foi realizada a modificação de superfície mediante troca de ligante com PAA e Cys. Isto permitiu remover os ligantes hidrofóbicos e fornecer grupo funcionais hidrofílicos na superfície das nanopartículas, garantindo sua redispersão em meios aquosos, além de proporcionar estabilidade coloidal a longo prazo.

Finalmente, as reações de acoplamento das nanopartículas hidrofílicas foi investigado através da formação de ligação covalente entre as UCNPs e as PLNPs funcionalizadas na superfície, com base na química de acoplamento EDC/NHS. Os resultados obtidos sugerem que a reação de acoplamento foi realizada com sucesso. Com tudo, são necessárias novas condições de acoplamento e caracterizações, bem como o estudo da transferência de energia entre as nanopartículas para melhor entendimento desse processo de acoplamento e para garantir futuras aplicações.

SYMBOL TABLE

$^1O_2$	Singlet oxygen
$^{2S+1}L_J$	Notation for energy levels
BG	Background
CB	Conduction band
CIE	Commission Internationale de l'Eclairage'
CR	Cross relaxation
CSU	Cooperative sensitization upconversion
CV	Crystal violet
Cys	Cysteamine
DC	Downconversion
DLS	Dynamic light scattering
DMF	N,N-Dimethylformamide
DRS	Diffuse reflectance spectra
DS	Downshifting
e^-	Electron
E1	First excited state
E2	Second excited state
EDC	1-Ethyl-3-(-3-dimethylaminopropyl) carbodiimide hydrochloride
EDS or EDX	Energy-dispersive X-ray spectroscopy
EDTA	Ethylenediaminetetraacetic acid
E_g	Band gap energy
EPR	Electron paramagnetic resonance
ESA	Excited-state absorption
ET	Energy transfer

ETU	Energy transfer upconversion
ExpDec2	Bi-exponential decay function
FEG-SEM	Field emission scanning electron microscope
FTIR	Fourier transform infrared
GO	Graphene oxide
GS	Ground state
h^+	Oxidative hole
$HO^{\bullet}$	Hydroxyl radical
HRTEM	High resolution transmission electron microscopy
$h\nu$	Photon energy
I_I	Integrated luminescence intensity
J	Electronic angular momentum
k	Photodegradation rate constant
L	Orbital angular momentum
LED	Light-emitting diode
Ln	Lanthanide
m	Number of electrons in 5d orbitals
MRI	Magnetic resonance imaging
n	Number of electrons in 4f orbitals
n	Number of the laser photons required to populate the upper emitting state
NHS	N-Hydroxysuccinimide
NIR	Near-Infrared
NPEGN	Poly(ethylene glycol) bis(amine)
$O_2^{\bullet-}$	Superoxide radical
OA	Oleic acid

OAm	Oleylamine
ODE	1-Octadecene
P	Pump laser power
PAA	Poly(acrylic acid)
PDI	Polydispersibility index
PDT	Photodynamic therapy
PEG	Poly(ethylene glycol)
PES	Polyethersulfone
PL	Persistent luminescence
PLE	Photoluminescence emission
PLNPs	Persistent luminescence nanoparticles
PS	Photosensitizer
PVP	poly(vinylpyrrolidone)
r	Average donor–acceptor distance
RE	Rare-earth
ROS	Reactive oxygen species
S	Total electron spin
SEM	Scanning electron microscopy
SNPs	Sacrificial nanoparticles
t or τ	Luminescence lifetime
t_1 or τ_1	First decay luminescence lifetime
t_2 or τ_2	Second decay luminescence lifetime
TEM	Transmission electron microscopy
UC	Upconversion or upconverting
UCL	Upconversion luminescence
UCNPs	Upconverting nanoparticles

UC-PL system	System resulting from the coupling of UC and PL materials
UCPs	Upconverting particles
UV	Ultraviolet
VB	Valence band
Vis	Visible
XRD	X-ray diffraction
ZGO	$ZnGa_2O_4:Cr^{3+}$
α-	Cubic phase of $NaLnF_4$
β-	Hexagonal phase of $NaLnF_4$
ζ potential	Zeta potential
λ_{em}	Emission wavelength
λ_{ex} or λ_{exc}	Excitation wavelength

LIST OF FIGURES

TABLE OF CONTENTS

CHAPTER 1

INTRODUCTION

1 INTRODUCTION

1.1 Luminescence materials

A luminescent material, also called a phosphor, is any substance capable of emitting electromagnetic radiation, usually accompanied by the emission of thermal radiation, after being externally excited by some type of energy, such as electromagnetic radiation (photoluminescence), energetic electron beams (catholuminescence), energy of a chemical reaction (chemiluminescence), mechanical energy (triboluminescence), electrical voltage (electroluminescence), among others.[1–4] The type of excitation energy indicates the type of luminescent material. For example, a photoluminescent material composed of a host lattice and an emitting center (activator) absorbs photons of light of a certain wavelength and emits photons of another wavelength, either longer [downshift (DS), downconversion (DC)] or shorter [upconversion (UC)].[2,3,5]

Although the emitting center can be directly excited by incident light, in most cases the function of a host lattice is to absorb that radiation and transfer it to the activator ion.[6]

Some characteristics of a good host matrix include high thermal and chemical stability, being transparent in the region of interest, having low to relatively low phonon energies, being resistant to photobleaching, etc.

Different inorganic materials have been widely used as host lattice, such as oxides, fluorides, phosphates, sulfides, silicates, aluminates, gallates, borates, aluminosilicates, selenides, sulfates, titanates, etc.[3,7–12]

The function of the emitting center or activator ion is mainly to emit photons, commonly in the UV, Visible and NIR regions. The most commonly used activators are lanthanide (Ln) ions such as Eu^{2+}, Eu^{3+}, Tb^{3+}, Er^{3+}, Tm^{3+}, Ho^{3+}, Nd^{3+}, Sm^{3+}, Dy^{3+} and Pr^{3+},[13–22] and some transition metal ions, such as Cr^{3+}, Cr^{4+}, Mn^{2+}, Mn^{3+}, Mn^{4+},[23–27] among others,[19,28] which have emission peaks mainly in the visible and NIR regions, suitable for several applications[28–34]

Since the absorption and emission properties of a luminescent material are generally determined by the type of host lattice and the characteristics of the activator ion, it is extremely important to choose them properly to ensure their successful

application. Similarly, the regions or wavelengths of excitation and emission for a given material also play a vital role for its appropriate and relevant use.

Typically, luminescent materials absorb and emit in the UV-Vis and Vis region, respectively. However, excitation and/or emission in the UV-Vis region presents some disadvantages for certain bioapplications, for example, various constituents of biological tissues absorb and/or emit significantly in this region, which leads to a very limited penetration depth of photons into biological tissues, as well as a high autofluorescence signal.[35–38]

Meanwhile, biological tissues show greater transparency in the NIR window (also called optical window or therapeutic window), between 650-950 nm (NIR-I), 1-1.35 µm (NIR-II), and 1.5-1.8 µm (NIR-III).[35–42] In addition, the autofluorescence signal is practically insignificant, because the chromophores present in the components of biological tissues are not excited by light beyond the visible region, making the development of materials that absorb and/or emit in those regions of the NIR highly interesting.[43–51]

Ln-doped materials with UC properties from NIR to UV-Vis-NIR, and materials presenting persistent luminescence (PL) properties with NIR emission have attracted great research attention in recent years due to their interesting optical properties and will be discussed in the next topics.

1.2 General introduction to trivalent lanthanide ions

Ln elements represent a group of 15 chemically similar elements in the periodic table from lanthanum (La) to lutetium (Lu), that are associated with the progressive filling of the 4f orbitals. These 15 elements, along with the chemically similar elements scandium (Sn) and yttrium (Y), are often collectively known as rare-earth (RE) elements (see Figure 1.1).[3,52–54]

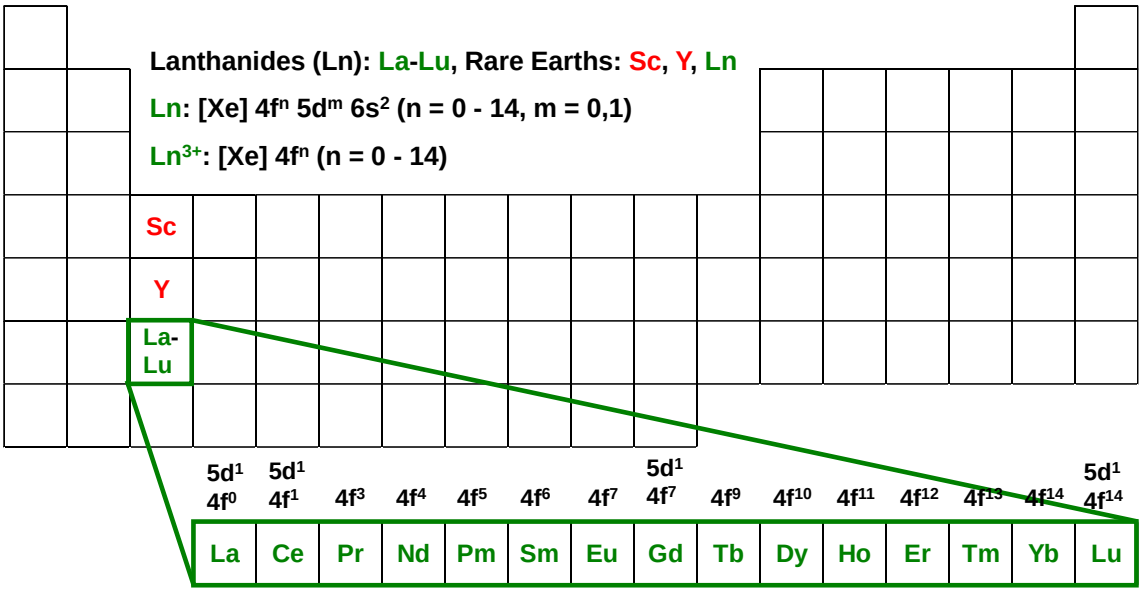

Figure 1.1 Position of the Ln elements and their chemically similar elements Sc and Y in the periodic table. Electronic configurations of neutral atoms and in the predominant oxidation state are included to highlight the progressive filling of the 4f orbitals.

Lanthanum (La), the first of the lanthanides, does not have electrons in the 4f subshell because it is higher in energy than the 5d subshell, so La has the electronic configuration [Xe] $6s^2 5d^1$, where [Xe] behaves like a "core". By progressively increasing the number of protons in the nucleus in the lanthanide series, the 4f orbitals contract towards the nucleus, decreasing their energy and becoming more stable and penetrating than the 5d orbital, so Cerium (Ce) has the electronic configuration [Xe] $4f^1 6s^2 5d^1$. From praseodymium (Pr) to europium (Eu), the progressive half-filling of the 4f orbitals occurs and there is no filling of the 5d orbital, so they all follow the configuration [Xe] $4f^n 6s^2$ (n = 3–7). After Eu, the pairing energy of electrons in the half-filled f orbitals is greater than the energy for filling the 5d orbital with an electron; therefore, for gadolinium (Gd) the next electron is added to the 5d orbital, and its configuration is [Xe] $4f^7 6s^2 5d^1$. From terbium (Tb) to ytterbium (Yb), increasing the number of protons in the nucleus leads to the previous pattern being resumed, and so all of them follow the configuration [Xe] $4f^n 6s^2$ (n = 9–14). Lu, which already has fully filled f-orbitals, has the configuration [Xe] $4f^{14} 6s^2 5d^1$.[2,52–55]

The most common and stable valence state of Ln or RE ions is the trivalent one (Ln^{3+}), for which they have an electronic configuration of [Xe] $4f^n$ (n = 0 - 14), which is energetically well separated from the [Xe] $4f^{n-1} 5d^1$ configuration ($\Delta E > 32{,}000\ cm^{-1}$). This configuration generate a wide variety of electronic levels (also called microstates), because each of the n electrons of the $4f^n$ configuration is associated with one of the

seven 4f wavefunctions and may have a spin of ± ½.[56] The way to associate the n electrons with the 4f orbitals, considering the spin, can be calculated using the expression:

$$\frac{(4l+2)!}{n!(4l+2-n)!} = \frac{14!}{n!(14-n)!} \quad \text{if } l = 3 \tag{1.1}$$

For example, the number of microstates for Tm^{3+}, electronic configuration [Xe] $4f^{12}$, is 91. Each energy level is characterized by three quantum numbers, S, L, and J, and is labeled as $^{2S+1}L_J$, according to Russel-Saunders' theory.[57] S denote the total electron spin, and results from the vector sum of the spins of the individual electrons. The value of S is used to obtain the total spin multiplicity according to the equation 2S + 1. For example, if S = 5, the multiplicity of the spectroscopic term or level is quintet. Meanwhile, L denote orbital angular momentum, and results from the sum of the magnetic orbital momentum of each individual electron. Each value of L is assigned a capital letter of the Latin alphabet to obtain the different spectroscopic terms: S (L = 0), P (L = 1), D (L = 2), F (L = 3), G (L = 4), H (L = 5), I (L = 6), K (L = 7), and so on. Vector addition of L and S affords the resulting quantum number, J, which can have values of (L + S), (L + S) – 1, ...(L − S).[57–59] Since the 4f orbitals do not directly participate in chemical bonding due to shielding effect by the fully filled 5s and 5p orbitals, their energy levels $^{2S+1}L_J$ are well defined and poorly sensitive to chemical environment.[6061] This shielding effect is mainly responsible for the luminescent properties associated with the forbidden 4f-4f transitions of the lanthanides ions, for example, their multiple narrow and sharp emission bands, long excited-state lifetimes, high resistance to photobleaching.

Furthermore, the highly complex energy levels of the lanthanide ions may be suitable for giving rise to several optical processes during electronic transitions, including DS, DC, and UC (Figure 1.2).[62–68] DS is a process that converts a high-energy excitation photon, usually in the UV, into a lower energy emission photon, usually in the visible region.[62–65] DC is a process in which one high-energy excitation photon, typically in the UV-Vis region, results in two or more lower-energy emission photons, commonly in the Vis-NIR region.[62,66] In particular, the UC process allows the conversion of two or more low energy excitation photons, usually in the NIR, to generate a higher energy emission photon, typically in the UV-Vis-higher energy NIR region.[62–65,67–69] Through these well-established optical processes, lanthanide ions can

have multiple and tunable emissions over a wide range of the electromagnetic spectrum, from UV to NIR.

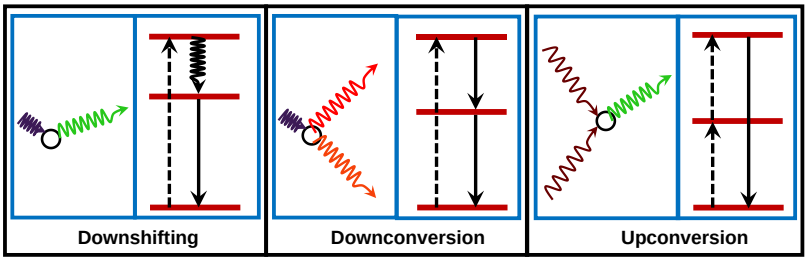

Figure 1.2 Simplified scheme of photon conversion processes.

1.3 Lanthanide-doped UC materials

Ln^{3+} ions can be incorporated as dopants into different nanomaterials including upconverting nanoparticles (UCNPs) to achieve unique luminescent optical properties. Ln^{3+}-doped UCNPs are diluted guest-host systems where Ln^{3+} ions are spatially distributed as guest in an appropriate dielectric crystal host lattice.[70] Typically, Ln^{3+}-doped UCNPs are composed of one or more sensitizer ions, with sufficiently large absorption cross-sections, and activators, which are optically active centers that produce emission when excited, e.g. Er^{3+}, Tm^{3+}, and/or Ho^{3+}. Interestingly, by proper control of Ln^{3+} dopants, UCNPs can emit at specific and tunable wavelengths, thus the color of the resulting emitted light can also be controlled.

1.3.1 UC Mechanisms

Several basic mechanisms have been identified by which UC luminescence (UCL) processes associated with Ln^{3+} ions can be achieved (Figure 1.3),[29,69,71–74] including:

1.3.1.1 Excited-state absorption (ESA)

For ESA process, Ln^{3+} ions with ladder-like energy levels, such as Er^{3+}, Tm^{3+}, Ho^{3+}, and Nd^{3+}, under 980 or 800 nm excitation, are often used. In this process, the Ln^{3+} ions in the ground state (GS) absorb photons and are promoted to the first excited state (E1), which must be a metastable level. Subsequently, the ions in E1 absorb another photon and are promoted to a second excited state E2, from which the ions decay to the ground state, emitting light of shorter wavelength.

1.3.1.2 Energy transfer upconversion (ETU)

The ETU process is probably the most studied today due to its high conversion efficiency. Basically, two different types of Ln^{3+} ions are needed in this process, sensitizers (usually Yb^{3+} or Yb^{3+}/Nd^{3+}) and activators (for example Tm^{3+}, Er^{3+} or Ho^{3+}). The successive absorption of two or more NIR photons by the sensitizer ions (ion 1), with subsequent energy transfer (ET) from the E1 of the sensitizer ions to the E1 (long-lived intermediate energy states of activator ions) and subsequent E2 of the activator ions (ion 2), is followed by the emission of higher energy photons than the excitation photons (NIR → UV-Vis-NIR).

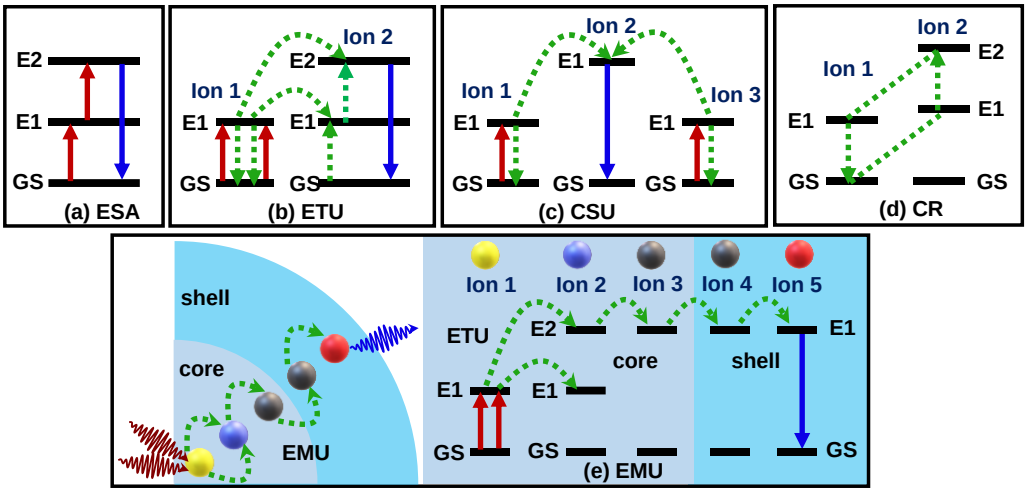

Figure 1.3 Schematic diagrams of different photon UC processes.

1.3.1.3 Cooperative sensitization upconversion (CSU)

CSU is a process that involves three ions, two sensitizers (ion 1 and 3), which are generally of the same type, and one activator (ion 2). This mechanism has been reported for materials containing Yb^{3+} ions as sensitizer and Pr^{3+}, Eu^{3+}, or Tb^{3+}, as activator ion. The process begins with the excitation of the sensitizer ions, which simultaneously transfer the excitation energy from their E1 to the E1 of the activator ion, resulting in the emission of light of wavelength shorter than the wavelength of the excitation light during radiative decay from the E1 to the GS of the activator ion. The activator ion does not have an intermediate energy level that matches the energy transferred by only one of the sensitizer ions, therefore, the efficiency of this process is very low.

1.3.1.4 Cross relaxation (CR)

CR is a process of energy transfer between two equal or different neighbor ions, but with similar energy differences between two energy levels of both, in such a way that an ion (ion 1) transfers its energy from an excited level E1 to a second ion (ion 2) that is already in its excited level E1. As a result, ion 1 decays to the GS (or to a lower energy excited level) and ion 2 is promoted to a higher energy excited level (E2). The process can be represented as E1 (ion 1) + E1 (ion 2) → GS (ion1) + E2 (ion 2). This process depends on the distance of the dopant ions and requires high concentrations of them. It should be noted that in general it is a detrimental process of luminescence extinction, however, in optimal concentrations of dopants it can help in other UC processes, for example, to populate the $^1D_2$ (and higher) state of Tm^{3+} ions, through the process of $^3F_{2,3}$ (Tm^{3+}) + $^3H_4$ (Tm^{3+}) → $^3H_6$ (Tm^{3+}) + $^1D_2$ (Tm^{3+}), during ETU.

1.3.1.5 Energy migration upconversion (EMU)

EMU has been reported for core/shell nanoparticles and starts with an ETU process between a sensitizer ion (ion 1) and an accumulator ion (ion 2) in the core domain. Subsequently, instead of being emitted, the energy is transferred to a migrator ion (ion 3). After that, the energy migrates through the core-shell interface by transfer between migrator ions (ion 3 - ion 4). Subsequently, ion 4 transfers the energy to an activator ion (ion 5), which finally decays radiatively, emitting a photon of shorter wavelength than the wavelength of the excitation photons. To avoid detrimental cross-relaxation processes, the sensitizer/accumulator and activator ions are spatially separated and confined in different layers of the core/shell structure. Usually Yb^{3+}, Tm^{3+}, and Gd^{3+} ions are incorporated as ions sensitizer, activator, and migrator ions, respectively, while Dy^{3+}, Sm^{3+}, Nd^{3+}, Eu^{3+}, Tb^{3+}, Ce^{3+} ions are commonly incorporated as activator ions (ion 5).[75–80]

In general, the UC process in this work refers to ETU mechanism, unless otherwise specified.

1.3.2 Design and fabrication of UCNPs

As UCL efficiency and the optical properties of UCNPs are generally affected by several parameters, such as types and concentration of dopant ions, host lattice, crystal phase as well as the architecture of the nanoparticles; this requires rationally designed UCNPs to ensure their successful use in various applications.[71,74,81–83]

1.3.2.1 Host lattice

The host lattice determines the local symmetry, the spatial distribution of the dopant Ln^{3+} ions, as well as the crystalline field strength in its environment, and consequently, the ability to relax Laporte-forbidden f–f transitions; therefore, its proper selection is essential to obtain high UCL efficiency. The selection of the host lattice material proceeds to fulfill a primordial set of criteria, including being transparent in the spectral range of interest, non-hygroscopic, chemically stable, and photobleaching resistant. Additionally, to achieve high UCL efficiency the host lattice must have low lattice phonon energies.[70,74,83–86]

Phonon-mediated non-radiative relaxation is one of the detrimental luminescence suppression pathways that affect the efficiency of the UC process.[87,88] The smaller the gap between two energy levels or the higher the energy of the phonons, the greater the probability that the phonons can fill the gap between them by multiphonon emission and, consequently, the probability of driving the excited electrons to the lower energy level without radiative emission.

Since many energy levels of the sensitizer and activator ions participate in the UC process, it is necessary for the host lattice to have sufficiently low phonon energies, especially when conversions of three or more photons are required. Although bromides and chlorides of Ln^{3+} generally exhibit low phonon energies, e.g., 175 and 240 cm^{-1}, respectively for $LaBr_3$ and $LaCl_3$,[89,90] they are generally highly hygroscopic, water soluble, and deliquescent, which limits their use as host lattices in UC processes.[90–92] In contrast, oxides, and phosphates of Ln^{3+} meet high chemical stability but their phonon energies are relatively high, e.g., 600, 700, and 1050 cm^{-1}, for Y_2O_3, Gd_2O_3, and $LaPO_4$, respectively,[89,93–95] leading to relaxation of the excited states by phonon-mediated nonradiative decays, and making the UC process inefficient. Fluoride-based host lattice systems, for example, $NaLnF_4$ and LnF_3, meet the prerequisite of chemical stability, non-hygroscopic nature, transparency in the UV-Vis-NIR region, resistance to photobleaching, as well as relatively low phonon energies (~350 cm^{-1}) to achieve high UC efficiency, thus are often used as host lattice materials for the synthesis of Ln-based UCNPs.[70,89,90,95–97]

As mentioned above, the local symmetry of the dopant ions at the lattice sites of the inorganic host material has a prominent impact on the optical properties of the UCNPs, which is correlated to the difference in crystal fields in the dopant ions vicinity

generated in different crystal symmetries. $NaYF_4$, $NaYbF_4$ and $NaGdF_4$, which are the most representative host lattice materials for UC, are known to crystallize in two different crystal phases,[67,98–104] the cubic phase (α-$NaLnF_4$) and the hexagonal phase (β-$NaLnF_4$). The last one is thermodynamically more stable at room temperature[98] and generally exhibits much stronger and sharper UCL, as well as higher quantum yield and UC efficiency than the cubic phase, due to the lower crystal symmetry which increases the 4f-4f transition probabilities by relaxing forbidden selection rules.[67,70,99,105] However, there is a greater tendency for the formation of the cubic rather than the hexagonal phase.[99,106–108] The cubic phase can be obtained at room temperature. However, obtaining the hexagonal phase requires a phase transition from the cubic one, demanding more energy because the free energy barrier for that phase transition is remarkably high.[99,106,107,109–111] In most cases, the hexagonal phase can be obtained by thermal treatment, which require elevated temperature conditions accompanied by long reaction times.

1.3.2.2 Dopant ions

Sensitizer and activator ions are mostly responsible for the UC process to occur, and their type and content can directly determine the efficiency of the process, as well as the color of the emitted light.[89,112–114] Sensitizer ions allow the UCNPs to absorb the excitation photons, while activator ions help in the UC process thanks to their ladder-like arrangement of levels with similar energy differences between them and relatively long lifetimes of their excited states, which allow the population of higher energy states, and the subsequent emission of higher energy photons.

Only a few sensitizer-activator ion pairs are suitable for UC process, including Yb^{3+}–Er^{3+}, Yb^{3+}-Tm^{3+}, and Yb^{3+}-Ho^{3+}, which can operate successfully under 980 nm thanks to the relatively large absorption cross section of Yb^{3+} ions in that region, due to the electronic transition $^2F_{7/2} \rightarrow {}^2F_{5/2}$.[70,89,90,96,112–114]

Additionally, several of the transitions between the ladder-like arranged energy levels of Er^{3+}, Tm^{3+} and Ho^{3+} ions are closely resonant with the $^2F_{7/2} \rightarrow {}^2F_{5/2}$ transition of Yb^{3+} ions, favoring the successive energy transfers between sensitizer and activator. In particular, Er^{3+} and Tm^{3+} ions have large enough energy gaps between various energy levels to decrease the probability of phonon-mediated nonradiative relaxation and increase the UC efficiency along with the probability of radiative transitions in the visible region for Er^{3+} ions and UV-Vis (blue)-NIR for Tm^{3+} ions (Figure 1.4).[74,81,115–117]

Er^{3+} ions have three main UCL emission bands, including a red emission band around 660 nm and two fairly close green emission bands around 525 and 545 nm, which involve the UC of two photons. During sample excitation, a first photon is absorbed mainly by Yb^{3+} ions through $^2F_{7/2} \rightarrow {}^2F_{5/2}$ transition. Yb^{3+} ions in the $^2F_{5/2}$ excited state transfer the energy nonradiatively to Er^{3+} ions in the $^4I_{15/2}$ GS, leading to the $^4I_{11/2}$ excited level population of Er^{3+} ions and the return of Yb^{3+} ions to $^2F_{7/2}$ GS. After that Er^{3+} ions can either decay nonradiatively to the $^4I_{13/2}$ excited state or be promoted to the $^2H_{5/2}$ excited state mediated by a second ET from excited Yb^{3+} ions after absorption of a new photon. Er^{3+} ions in the $^2H_{5/2}$ excited state decay nonradiatively to either the $^2H_{11/2}$ state (responsible for emission at 525 nm) or the $^4S_{3/2}$ state (responsible for emission at 545 nm) (Figure 1.4). Similarly, Er^{3+} ions in the $^4I_{13/2}$ excited state can be promoted to the $^4F_{9/2}$ excited state (responsible for emission at 660 nm) after a second ET from the excited Yb^{3+} ions. The radiative decay from $^2H_{11/2}$, $^4S_{3/2}$, and $^4F_{9/2}$ excited states to the $^4I_{15/2}$ GS of Er^{3+} ions produces the characteristic green and red emissions of these ions, according to the literature.[118–121]

Meanwhile, the main UC emission bands of the Tm^{3+} ions are located in the NIR (~800 nm), blue (around 475 and 450), and UV (near 360, 345, and 290 nm) regions, for this reason Tm^{3+}-doped UCNPs are suitable for applications in deep tissues bioimaging or in the activation of photocatalysts, photosensitizers (PS), or PL nanoparticles (PLNPs).

As in the UC mechanism based on Er^{3+} ions, the UC process based on Tm^{3+} ions starts with the absorption of the excitation light at 980 nm by Yb^{3+} ions leading to population of the excited state ($^2F_{5/2}$) as a result of the $^2F_{7/2} \rightarrow {}^2F_{5/2}$ transition. The excited Yb^{3+} ions transfer their energy to Tm^{3+} ions through successive energy transfer (ET) steps, resulting in the population of its higher energy levels. The excited Tm^{3+} ion then relaxes by emitting upconverted photons of shorter wavelengths (than the excitation wavelength of 980 nm) at around 290, 345, 360, 450, 475, and 800 nm which are, respectively, attributed to the $^1I_6 \rightarrow {}^3H_6$, $^1I_6 \rightarrow {}^3F_4$, $^1D_2 \rightarrow {}^3H_6$, $^1D_2 \rightarrow {}^3F_4$, and $^1G_4 \rightarrow {}^3H_6$ transitions of Tm^{3+} ions (Figure 1.4).[105,122–124]

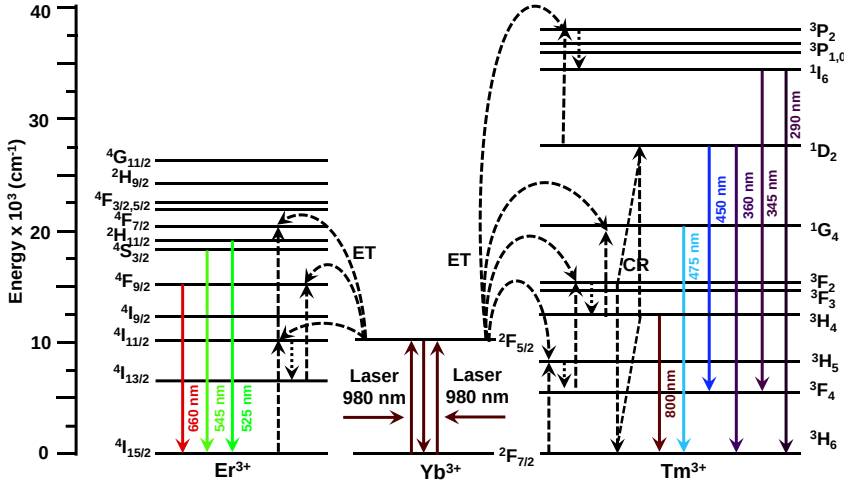

Figure 1.4 Schematic diagram of the mechanism of the UC process between the Yb^{3+}–Er^{3+} and Yb^{3+}–Tm^{3+} pairs involving their energy level diagrams to explain the main UC emissions of the Er^{3+} and Tm^{3+} ions. ET: Energy transfer; CR: Cross relaxation.

It is worth mentioning that increasing the concentration of sensitizer and activator ions will always lead to an increase in the UCL intensity of UCNPs. Of course, higher the concentration of Yb^{3+} ions, greater the intrinsic absorption cross-section of the UCNPs. However, a very high concentration of Yb^{3+} ions could lead to non-radiative relaxation by energy migration to quenching sites on UCNPs surface.[125–127]

On the other hand, although the increase in activator ions concentration shortens the distance between sensitizer-activator ions, a highly doped system with activator ions irremediably leads to deleterious cross-relaxation processes and, consequently, to non-radiative decay;[84,125–127] therefore, an adequate control of the elemental composition of UCNPs is essential to avoid energy losses due to non-radiative decay and maximize the emissions of upconverted photons.[29,128,129]

In addition, doping a suitable host material with different types of activators (e.g., Er^{3+}/Tm^{3+}) in conjunction with Yb^{3+} as the sensitizer, ensuring precise control of their concentration, can produce multicolor UCL under 980 nm diode laser excitation.[113,117,130–132] However, this strategy can also lead to cross-relaxation processes between the different types of activators, resulting in low UCL efficiency.

To address the problem of non-radiative decay associated with energy migration to quenching sites on UCNPs surface and achieve multicolor UCL by simultaneous doping with different activator ions it is necessary to design the nanoparticle with a core/shell architecture,[133–135] where the protective shell prevents the migration of energy from Yb^{3+} ions in the core region to quenching sites on nanoparticle surface, in

addition to allowing the activator ions to be separated into two different domains, the core and shell region.

1.3.2.3 Nd^{3+}-sensitized core/shell/shell UCNPs

In the Yb^{3+}-sensitized UC process, the excitation wavelength (980 nm) may be strongly absorbed by water molecules in biological environment, which could cause local heating problems in the vicinity of cells and tissues, thus damaging them.[136] To solve this problem, some research has been focused on the extension of the UC excitation spectrum to shorter wavelengths (especially, in the vicinity of 808 nm using Nd^{3+} ions as sensitizers), where water molecules do not absorb significantly.[136–143]

Nevertheless, efficient multicolor UCL output from Nd^{3+}-sensitized UCNPs remains vague until this point. The UC mechanism under 800 nm laser excitation differs basically from the UC mechanism based on the excitation of Yb^{3+} ions under 980 nm laser irradiation in the first step. Specifically, the electrons of Nd^{3+} ion in the $^4I_{9/2}$ GS are excited to the $^4F_{5/2}$ level by the 808 nm laser. After a non-radiative decay of Nd^{3+} ions from the $^4F_{5/2}$ excited level to the $^4F_{3/2}$ excited level, an energy transfer occurs between the excited Nd^{3+} ions and the Yb^{3+} ions in the GS, causing the population of the excited level $^2F_{5/2}$ of Yb^{3+} ions and the return of Nd^{3+} ions to the GS (Figure 1.5).[141] After that, the energy transfer from the Yb^{3+} ions to the activator ions occurs as mentioned above.

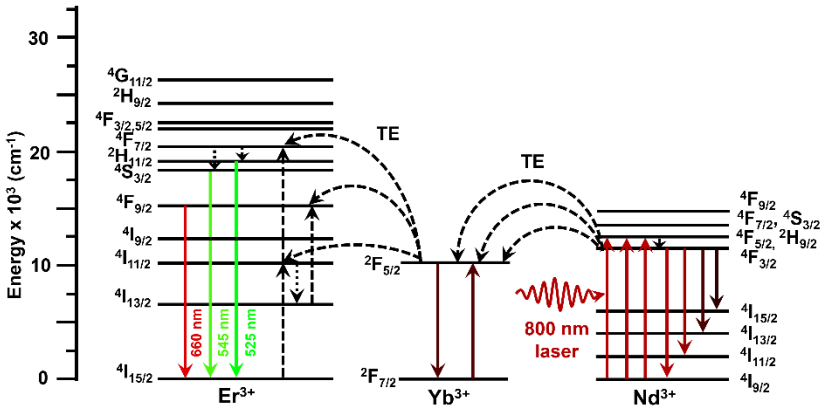

Figure 1.5 Schematic illustration of the UC process involving Nd^{3+}, Yb^{3+}, and Er^{3+}, based on the excitation of Nd^{3+} ions at 800 nm.

In Chapter 3 of this work, Nd^{3+}-sensitized UCNPs, using $NaGdF_4$ as host matrix, are further explored, and a detailed study of the synthesis is conducted, controlling the core/multishell architecture and the lanthanide contents to obtain multicolor UCL. Such

tunable multicolor UCL emission makes these Nd^{3+}-sensitized Gd^{3+}-based core/multishell UCNPs potential candidates for bioimaging and magnetic resonance imaging (MRI) dual modal application.

1.3.3 Synthesis of UCNPs

The optical properties and, in general, the successful application of UCNPs in different fields, depend largely on obtaining monodisperse UCNPs, with adequate control of size, shape, elemental composition, and crystalline phase during synthesis.

The most common methods for the synthesis of high-quality Ln^{3+}-doped core-only, core/shell, and core/multishell UCNPs include high-temperature coprecipitation and thermal decomposition methods, hot-injection strategies, and conventional and microwave-assisted hydrothermal treatment,[8,13,122,144–148]

Additionally, the seed-mediated growth via high-temperature co-precipitation route and ripening-mediated self-focusing method for layer-by-layer epitaxial shell growth allow optimal control of the growth of one or more layers on the core (seed) nanoparticles and obtain high-quality core/shell and/or core/multishell structured UCNPs.[135,149–151]

For developing of this thesis, high-temperature co-precipitation methods, microwave-assisted hydrothermal treatment, seed-mediated growth via high-temperature co-precipitation route and ripening-mediated self-focusing method with injections of small sacrificial nanoparticles for layer-by-layer epitaxial shell growth were followed, and therefore, only the fundamentals of these methods will be described here.

1.3.3.1 High-temperature coprecipitation method for the synthesis of core UCNPs

High-temperature coprecipitation method for the synthesis of UCNPs is based on the formation of small amorphous coprecipitates of fluoride-based nanoparticles at room temperature, followed by growth and ripening at high temperatures (280-315 °C) for a relatively short time, ranging from minutes to a few hours. Although other co-precipitating (stabilizing) agents/high boiling solvents could also be used, oleic acid (OA) as the stabilizing agent and 1-octadecene (ODE) as the solvent are the most widely used as they allow obtaining uniform, high-quality UCNPs and because of their cost-effectiveness, biocompatibility, and efficiency[133,152–154]

1.3.3.2 Microwave-assisted hydrothermal treatment for the synthesis of core UCNPs

Hydrothermal treatment is a synthesis strategy that employs a Teflon-lined sealed autoclave reactor that allows obtaining UCNPs from aqueous solutions of the precursors at lower temperatures (180–220 °C) than those needed in the high-temperature coprecipitation method, but with much longer reaction times (12–24 h) and much higher pressures (0.3–4 MPa).

In addition, the microwave-assisted hydrothermal approach is a fast and simple method that drastically reduces the reaction time (0.5–1 h), even at temperatures lower than 200 °C. It also provides an excellent control over experimental parameters and a uniform distribution of energy inside the sample due to the high penetrability of microwave radiation, achieving a low thermal gradient and uniform heating. Micrometric size UC particles (UCPs), which can be used in heterogeneous photocatalysis processes for the activation of photocatalysts under NIR excitation, can be synthesized by microwave-assisted hydrothermal treatment.[105,122]

1.3.3.3 Methodologies for the synthesis of core/shell and core/multishell UCNPs

Epitaxial shell growth on UCNPs is a widely used strategy to spatially separate the optically active core from the surrounding environment, reducing non-radiative decays caused by energy migration to quenching sites on its surface and improving the efficiency of the UC process. Furthermore, shell growth is an attractive option to fabricate UCNPs with multifunctionality.

1.3.3.3.1 Seed-mediated growth via high-temperature co-precipitation route

This strategy is a powerful and versatile approach to synthesize high quality core/shell structure UCNPs with a relatively uniform morphology and size. Similar to the high temperature coprecipitation method, this is based on the coprecipitation of lanthanide fluorides and their subsequent growth and ripening at high temperatures, but in this case the coprecipitation is carried out in the presence of small crystals as seeds (core UCNPs), which are used as seed nuclei for the epitaxial growth of the outer shell layer.[76,151] However, in the widely used seed-mediated shell growth on β-$NaLnF_4$, the shell precursors preferentially nucleate as α-$NaLnF_4$ and thus a ripening-mediated process is necessary to lead to the formation of β-core/β-shell UCNPs. By consecutively repeating the coprecipitation/ripening of new precursors using the

core/shell nanocrystals as seeds, it is possible to obtain UCNPs in core/multishell architecture. The shell thickness can be controlled by controlling the molar ratio of core to shell precursor.[153,154]

1.3.3.3.2 Ripening-mediated self-focusing method for layer-by-layer epitaxial shell growth

This approach consists in that larger particles with smaller surface-to-volume ratios are favored over energetically less stable smaller particles, resulting in the growth of larger particles at the expense of smaller ones. When small *α*-phase nanoparticles, called sacrificial nanoparticles (*α*-SNPs), are injected at high temperature into a mixture containing OA, ODE, and larger *β*-phase core UCNPs (defocusing process), the thermodynamically less stable *α*-SNPs dissolve rapidly, forming shell monomers. The fast release of these monomers results in a supersaturation of monomers which are then deposited on the larger stable core nanoparticles forming the *β*-core/*β*-shell structure (self-focusing). The most interesting point of this approach comes mainly from the high degree of control that can be achieved over the size, shape, and structure of the UCNPs without the need for vigorous control during synthesis. Additionally, this strategy saves time by repeating the defocusing and self-focusing cycle, which allow layer-by-layer growth during the same synthesis, enabling to evaluate the shell thickness and synthesize core/multishell UCNPs more efficiently.[150]

1.3.4 Surface Modification

Most of the synthetic methodologies mentioned above produce UCNPs with hydrophobic surfaces, exclusively dispersible in nonpolar organic solvents, due to the hydrophobic nature of the capping ligands used during the synthesis (*e.g.*, OA). The resulting non-dispersibility nature of these nanoparticles in aqueous media limits their use in bioapplications, where hydrophilicity is essential.

Since surface properties determine the biocompatibility of nanoparticles *in vitro* and *in vivo*, a crucial step in the use of UCNPs in bioapplications is the surface hydrophilic modification to make them water-dispersible, provide both a stable aqueous colloidal dispersion, and anchor suitable ligands to the surface for subsequent conjugation with biomolecules and/or other ligands.

A wide variety of surface modification strategies have been developed to fulfill this prerequisite and can be categorized into four groups: chemical modification of the

original hydrophobic ligand on the surface, amphiphilic coatings, encapsulation with inorganic materials forming a hydrophilic shell and complete exchange of the original ligand by another.[155–160]

Here only the ligand exchange strategy will be discussed since it was the only one used in the development of this thesis, and because it is usually the simplest, fastest, and most cost-effective strategy.

1.3.4.1 Ligand exchange strategy

Ligand exchange is a versatile strategy for modifying the surface of UCNPs, which is usually quite simple, fast, and cost-effective. It is based on the replacement of the original hydrophobic ligands by others of a hydrophilic nature. Ligand exchange can be achieved in two ways: by direct exchange of the original hydrophobic ligands for the new ones and by two-step strategies using $NOBF_4$ (or acid treatment with HCl) to remove the hydrophobic ligands, followed by coating with the new hydrophilic ones.[155–157,161]

1.3.4.1.1 Direct exchange of the original hydrophobic ligands

For this purpose, ligands that have a higher coordination capacity with the lanthanide ions than the original ligands are used, in many cases in excess. The protocols are quite simple, but the elaboration is tedious and more challenging than the chemical reaction itself. Typically, oleate-capped UCNPs and the hydrophilic ligands are mixed in a suitable solvent under continuous stirring, generally at high temperature for a few hours or days.

A major disadvantage is that protocols must be optimized for each type/family of ligands because each requires specific reaction conditions. Furthermore, the particles tend to agglomerate during ligand exchange.[155,162]

1.3.4.1.2 Two-step strategies

This is a widely applicable strategy for nanoparticle surface modification. In a first step, the hydrophobic ligands are removed from the surface of UCNPs in the presence of an excess of $NOBF_4$, resulting in the stabilization of the nanoparticles by BF_4^- ions. Although the nanoparticles are stabilized by BF_4^- ions instead of NO^+ ions, the

participation of the latter is important, since it has been shown that other fluoroborates work much less well, or even not at all in this strategy.

Total exchange of OA molecules by BF_4^- ions usually takes 20 minutes or less at room temperature, without the use of large amounts of solvents, requiring only stirring or sonication, thus resulting in an easy, fast, and cost-effective method, as well as being a general ligand-exchange strategy that may also be applied to other types of nanoparticles and enables their sequential surface functionalization.

In addition to the above, the aggregation during the ligand exchange process is considerably reduced compared to other protocols, and the resulting nanocrystal dispersions in aprotic polar solvents such as dimethylformamide (DMF) have long-term colloidal stability.[157]

In a second step, by simply adding and stirring, new molecules or polymers with functional groups of a hydrophilic nature can be anchored to the surface of the nanoparticles, resulting in the exchange of BF_4^- ions for new ligands, such as poly(acrylic acid) (PAA), poly(vinylpyrrolidone) (PVP), poly(ethylene glycol) (PEG), citrate, etc.[157,163]

1.3.5 Application of UCNPs and UCPs

The unique luminescent properties of UCNPs and UCPs make them attractive for various interesting bioapplications, such as nanothermometry, photoluminescence bioimaging, in bioassays for the detection of viruses, bacteria, and cancer cells, treatment of some diseases including cancer, photoinduced drug delivery, etc.[164–169] Furthermore, Ga^{3+}-based UCNPs can be used as dual-mode imaging contrast agents.[170]

In addition to their multiple bioapplications, UCNPs and UCPs can also be used in heterogeneous photocatalysis, to obtain UV-Vis-NIR active broad-spectrum photocatalytic systems by coupling UCNPs or UCPs with UV-Vis active photocatalysts, since the emitted photons by the UC materials in the UV-Vis region can activate photocatalysts with appropriate bandgap energy.[105,122,171] Furthermore, the combination of broad-spectrum photocatalytic systems with other advanced oxidation processes, including the heterogeneous Fenton-like process, seems a highly promising strategy to achieve more efficient degradation results, and even to improve the photostability of photoinstable photocatalysts, such as Ag_3PO_4, which has high photocatalytic activity, but suffers from photoreduction when exposed to UV-Vis light.

The two main objectives of Chapter 4 of this work were (i) the development of a broad-spectrum photocatalytic system by combining UCPs with Ag_3PO_4, photocatalyst, and (ii) the improvement of Ag_3PO_4 photostability using H_2O_2, which allows Ag_3PO_4 oxidation back/regeneration while leading to the formation of reactive oxygen species through Fenton-like reactions.

Moreover, increasing attention has been paid to the use of UCNPs in the activation of PL materials,[172,173] to simultaneously explore the advantages offered by the individual use of each of the two types of materials. For example, excitation of UCNPs at NIR allows deep penetration into biological tissues, while afterglow emission of PL materials could prevent damage to biological tissues by avoiding the continuous use of the excitation laser irradiation.

1.4 PL materials

PL materials, also called long-lasting or afterglow materials, have drawn considerable attention in the field of luminescence bioimaging and other bioapplications since they allow decreasing the exposure time of tissues to the excitation radiation, in addition to considerably reducing the autofluorescence background signal.[174–176] This is due to the inherent ability of PL materials to function as optical batteries, storing excitation energy and eventually emitting lower energy photons for a long time after removing the excitation source, which in many cases can even be seen with the naked eye for several hours.

Generally, two kinds of active centers are involved in PL process: traps and emitters. Trap levels originate because of lattice defects, impurities, or co-dopants in the material, mainly just below the conduction bands.[177–179]

Excitation with suitable energy leads to the separation of electron-hole pairs, forming holes in the valence band and electrons in the conduction band, the latter are captured in the trap levels.

The traps operate as deposits that store the excitation energy. When the excitation light is switched off, the charge carriers are gradually released from such traps and recombine radiatively or non-radiatively with the emitters (e.g., activator dopant ions) to emit PL[177,180] as schematically shown in Figure 1.6.

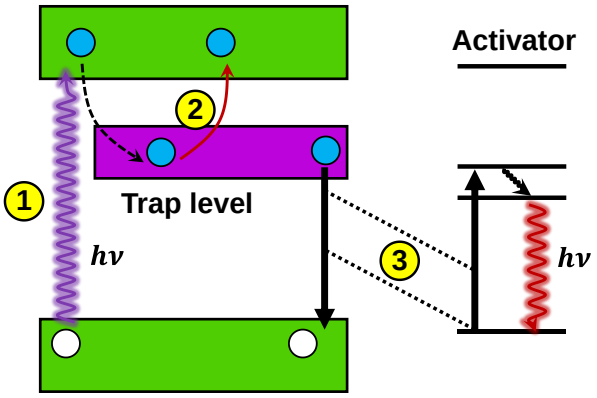

Figure 1.6 Schematic representation of a PL mechanism.

The characteristics of the emission center mainly determine the emitting wavelength region of interest, while those of the trap center determine the intensity and duration of PL.[179,181]

Various types of lattice defects such as cation or anion substitution, interstitial impurities, cation or anion vacancies, and antisites act as electron and hole traps in the host material (Figure 1.7).[182,183]

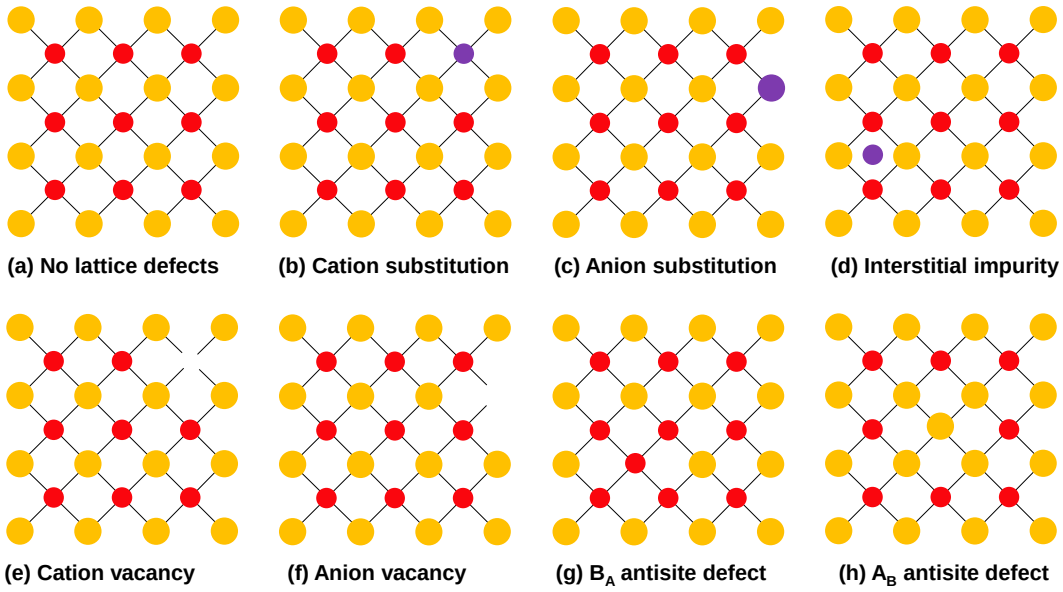

Figure 1.7 Examples of different types of point defects in a crystal lattice.

Emission centers can be lanthanide ions (e.g., Ce^{3+}, Eu^{2+}, Nd^{3+}, Er^{3+}, Pr^{3+}, Sm^{3+}) with 5d → 4f or 4f → 4f transitions, transition metal ions (e.g., Cr^{3+}, Mn^{2+}, Mn^{4+}, Ni^{2+}) with d → d transitions, or other metal ions (e.g., Pb^{2+}, Bi^{3+}) with p→s transitions, etc. However, only a few have PL emissions in the NIR region.[177,179,181,184]

Cr^{3+}-doped gallates such as $ZnGa_2O_4:Cr^{3+}$ (ZGO) have recently paid important attention as highly promising PL materials for application as contrast agents for long-term *in vivo* luminescence-based optical imaging[23,174,185,186] due to their long-lasting emission in the NIR-I around 700 nm originating from the $^2E_g \rightarrow {}^4A_{2g}$ transition of Cr^{3+} emitters, according to Tanabe-Sugano diagram (Figure 1.8).[187,188]

Furthermore, the excitation of ZGO is not only limited to the ultraviolet region, like most afterglow phosphors, but it can also be excited by X-rays and visible light, increasing the interest of researchers for its use in various applications.[189–192]

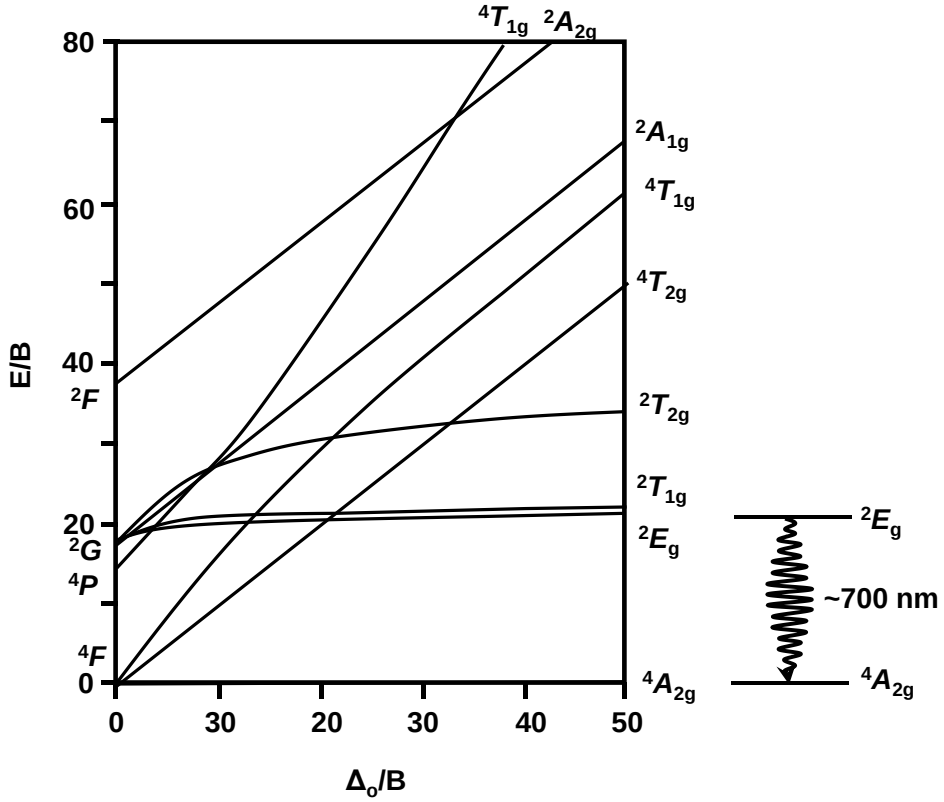

Figure 1.8 Tanabe-Sugano diagram for Cr^{3+} ion in octahedral geometry (left) and ^2E_g and $^4A_{2g}$ energy states involved in Cr^{3+} ion emission around 700 nm (right).

Nevertheless, several challenges to ensure the application of these materials in bioapplications remain unresolved. One of the major challenges related to the use of PL materials in bioapplications is the lack of crystal size control, since high calcination temperatures (above 1000 °C) are needed to induce lattice defect formation and increase PL signal, leading to exaggerated particle growth and poor size distribution.[12,193–195] In addition, the large size of the particles and the lack of ligands on the surface make their redispersion in aqueous media practically impossible.

These challenges have been the subject of various studies in recent years. For example, by combining sol-gel and calcination procedures, several researchers obtained PL nanomaterials at lower temperatures (around 1000 °C), but the problem of agglomeration remained unsolved.[196,197]

Particularly, hydro(solvo)thermal treatments allow obtaining ZGO particles at much lower temperatures. In addition, they offer the possibility of obtaining PL nanoparticles (PLNPs) with better control of size and morphology, thus being of greater relevance for bioapplications.[189,198–201]

Until now, the hydro(solvo)thermal strategies that allow better control of size and morphology in the synthesis of PLNPs and other nanomaterials are those that use long-chain fatty acids, such as OA, to coat the nanoparticles,[189,199–201] since a lower degree of polydispersity is obtained and agglomeration between them can be avoided, as mentioned above for the synthesis of UCNPs.

Srivastava *et al*.[199] obtained 6.1 nm ZGO nanoparticles through a biphasic synthesis route, heating a mixture formed by an aqueous solution of $Zn(NO_3)_2$, $Ga(NO_3)_3$ and $Cr(NO_3)_3$ and an organic solution of OA and toluene at 160 °C in an autoclave reactor. However, there was still a need for subsequent calcination at 750 °C to obtain PL emission.

Also using OA as a stabilizing agent, Yeh *et al*.[189] synthesized ZGO concave nanocubes with an edge length of 30 nm through a solvothermal process at 220 °C, which showed afterglow emission for more than 6 h without the need for additional calcination.

Similarly, Chen *et al*.[200] synthesized ZGO PLNPs by a liquid-solid-solution hydro(solvo)thermal method at 210 °C using $Zn(NO_3)_2$, $Ga(NO_3)_3$, $Cr(NO_3)_3$, and a mixture of OA, ethanol, water, and sodium hydroxide. Due to the oleate molecules on the surface the PLNPs produced were monodisperse and flexible for surface functionalization, however they emphasized that their optical properties need to be improved.

More recently, Gao *et al*.[201] reported a solvothermal synthesis route, based on methanol-mediated pyrolysis of zinc, gallium, and chromium acetylacetonates to synthesize size-adjustable ZGO in a mixture of OA and ODE. Interestingly, the authors used smaller nanoparticles as seeds to obtain larger nanoparticles by seed-mediated growth, which allowed them to achieve an almost 10-fold increase in luminescence lifetime. They concluded that the increase in size favors the storage and release of

electrons captured by relatively deep traps, which leads to an increase in the luminescence lifetime (τ).

In addition to the controlled synthesis of ZGO PLNPs with suitable morphological characteristics and good optical properties, other prerequisites must be resolved before the proper use of these nanocrystals in bioapplications. For example, nanoparticles must have good redispersibility in aqueous media, long-term colloidal and gravitational stability, and functional groups anchored to their surface to enable their subsequent conjugation with biomolecules.

In Chapter 5 of this thesis, hydrophilic NIR-emitting ZGO PLNPs with improved afterglow properties that fulfill several fundamental requirements for optical bioapplications were obtained; therefore, the aforementioned challenges were well addressed here.

In addition to the advances related to the development of PLNPs suitable for bioapplications obtained in this thesis, these ZGO PLNPs may be appropriate for coupling with UCNPs to develop biocompatible UC-PL systems, thus opening new research horizons.

1.5 NIR-activated PL materials

Taking into account the above considerations on the advantages of using near-infrared excitation/emission in bioapplications, the interesting optical properties of UCNPs, and the inherent ability of PL materials to function as optical batteries and emit for a long post-excitation time, the development of UC-PL systems activated by NIR radiation and presenting PL in the NIR has attracted great research interest.[172,173]

A great advantage of developing UC-PL materials is the possibility of obtaining NIR-rechargeable “optical batteries”, which can find interesting applications including the activation of PS in photodynamic therapy (PDT) or deep tissue luminescence bioimaging.

Unlike conventional PDT, for example, a UC-PL-PS system achieves a deeper penetration of the excitation light (980 nm laser), which is absorbed and upconverted by the UC materials. The photons emitted in the UV-Vis region by the UC materials activate the PL materials, which continue to emit for a long post-excitation period after which a new recharge takes place. In parallel, the photons emitted by the PL materials

lead to the excitation of PS responsible for producing singlet oxygen ($^1O_2$) capable of killing cancer cells.

However, most of the works published so far on the subject use PL materials obtained by calcination at high temperatures and even UCPs with several micrometers in size, which makes their real use in bioapplications practically impossible.[173,202,203]

Therefore, it is of paramount importance to develop novel UC-PL systems that are properly sized and fulfill the fundamental prerequisites for their potential bioapplications.

For this reason, the NIR-emitting PLNPs obtained in Chapter 5 of this work have been used in conjunction with sub-40 nm size UCNPs obtained in Chapter 6 of this work to investigate their coupling in order to develop a UC-PL system with suitable properties for bioapplications.

1.6 References

(1) Ugemuge, N.; Parauha, Y. R.; Dhoble, S. J. Synthesis and Luminescence Study of Silicate-Based Phosphors for Energy-Saving Light-Emitting Diodes. In *Energy Materials: Fundamentals to Applications. Elsevier*, **2021**, 445–480.

(2) Blasse, G.; Grabmaier, B. C. A General Introduction to Luminescent Materials. In *Luminescent Materials*. *Springer*, **1994**.

(3) Ronda, C.;Jüstel, T.; Nikol, H. Rare earth phosphors: fundamentals and applications. *J. Alloys Compd.* **2017**, *275–277*, 185–196.

(4) Belsky, A.N.; Krupa, J.C. Luminescence excitation mechanisms of rare earth doped phosphors in the VUV range. *Displays* **1999**, *19*, 6901–6904.

(5) DeLuca, J. A. An Introduction to Luminescence in Inorganic Solids. *J. Chem. Educ.* **1980**, *57*, 541.

(6) Wang, F.; Liu, X. Rare-Earth Doped Upconversion Nanophosphors. In *Comprehensive Nanoscience and Nanotechnology* **2011**, 1, 359–384.

(7) Lee, S. H.; Choi, J. I.; Kim, Y. J.; Han, J. K.; Ha, J.; Novitskaya, E.; Talbot, J. B.; McKittrick, J. Comparison of Luminescent Properties of Y_2O_3:Eu^{3+} and $LaPO_4$:Ce^{3+}, Tb^{3+} Phosphors Prepared by Various Synthetic Methods. *Mater. Charact.* **2015**, *103*, 162–169.

(8) Nigoghossian, K.; Ouellet, S.; Plain, J.; Messaddeq, Y.; Boudreau, D.; Ribeiro, S. J. L. Upconversion Nanoparticle-Decorated Gold Nanoshells for near-Infrared Induced Heating and Thermometry. *J. Mater. Chem. B* **2017**, *5*, 7109–7117.

(9) Rodríguez Burbano, D. C.; Rodríguez, E. M.; Dorenbos, P.; Bettinelli, M.; Capobianco, J. A. The Near-IR Photo-Stimulated Luminescence of CaS:Eu^{2+}/Dy^{3+} Nanophosphors. *J. Mater. Chem. C* **2014**, *2*, 228–231.

(10) Petrovykh, K. A.; Rempel, A. A.; Kortov, V. S.; Buntov, E. A. Sol-Gel Synthesis and Photoluminescence of Zn_2SiO_4:Mn Nanoparticles. *Inorg. Mater.* **2015**, *51*, 152–157.

(11) Priya, R.; Negi, A.; Singla, S.; Pandey, O. P. Luminescent Studies of Eu Doped $ZnAl_2O_4$ Spinels Synthesized by Low-Temperature Combustion Route. *Optik* **2020**, *204*. 164173.

(12) Bessière, A.; Jacquart, S.; Priolkar, K.; Lecointre, A.; Viana, B.; Gourier, D. $ZnGa_2O_4:Cr^{3+}$: A New Red Long-Lasting Phosphor with High Brightness. *Opt. Express* **2011**, *19*, 10131–10137.

(13) Nigoghossian, K.; Messaddeq, Y.; Boudreau, D.; Ribeiro, S. J. L. UV and Temperature-Sensing Based on $NaGdF_4:Yb^{3+}:Er^{3+}@SiO_2$-$Eu(Tta)_3$. *ACS Omega* **2017**, *2*, 2065–2071.

(14) Lima, L. R.; Moraes, M. L.; Nigoghossian, K.; Peres, M. F. S.; Ribeiro, S. J. L. Silk Fibroin-Antigenic Peptides-$YVO_4:Eu^{3+}$ Nanostructured Thin Films as Sensors for Hepatitis C. *J. Lumin.* **2016**, *170*, 375–379.

(15) Nigoghossian, K.; Miyashita, T.; Omura, A.; Yeroslavsky, G.; Kim Dung, D. T.; Okubo, K.; Umezawa, M.; Kamimura, M.; Soga, K. Infrared to Visible Upconversion Luminescence of Trivalent Erbium Tetrafluoroborate Complexes. *Opt. Mater. Express* **2020**, *10*, 1749–1766.

(16) Nigoghossian, K.; Kulakova, A. N.; Félix, G.; Khrustalev, V. N.; Shubina, E. S.; Long, J.; Guari, Y.; Sene, S.; Carlos, L. D.; Bilyachenko, A. N.; Larionova, J. Temperature Sensing in Tb^{3+}/Eu^{3+}-Based Tetranuclear Silsesquioxane Cages with Tunable Emission. *RSC Adv.* **2021**, *11*, 34735–34741.

(17) Dutczak, D.; Jüstel, T.; Ronda, C.; Meijerink, A. Eu^{2+} Luminescence in Strontium Aluminates. *Phys. Chem. Chem. Phys.* **2015**, *17*, 15236–15249.

(18) Shi, R.; Xu, J.; Liu, G.; Zhang, X.; Zhou, W.; Pan, F.; Huang, Y.; Tao, Y.; Liang, H. Spectroscopy and Luminescence Dynamics of Ce^{3+} and Sm^{3+} in $LiYSiO_4$. *J. Phys. Chem. C* **2016**, *120*, 4529–4537.

(19) Drabik, J.; Cichy, B.; Marciniak, L. New Type of Nanocrystalline Luminescent Thermometers Based on Ti^{3+}/Ti^{4+} and Ti^{4+}/Ln^{3+} (Ln^{3+} = Nd^{3+}, Eu^{3+}, Dy^{3+}) Luminescence Intensity Ratio. *J. Phys. Chem. C* **2018**, *122*, 14928–14936.

(20) Pedroso, C. C. S.; Carvalho, J. M.; Rodrigues, L. C. V.; Hölsä, J.; Brito, H. F. Rapid and Energy-Saving Microwave-Assisted Solid-State Synthesis of Pr^{3+}-, Eu^{3+}-, or Tb^{3+}-Doped Lu_2O_3 Persistent Luminescence Materials. *ACS Appl. Mater. Interfaces* **2016**, *8*, 19593–19604.

(21) Sun, L.; Qiu, Y.; Liu, T.; Zhang, J. Z.; Dang, S.; Feng, J.; Wang, Z.; Zhang, H.; Shi, L. Near Infrared and Visible Luminescence from Xerogels Covalently Grafted with Lanthanide [Sm^{3+}, Yb^{3+}, Nd^{3+}, Er^{3+}, Pr^{3+}, Ho^{3+}] β-Diketonate Derivatives Using Visible Light Excitation. *ACS Appl. Mater. Interfaces* **2013**, *5*, 9585–9593.

(22) Zou, Q.; Marcelot, C.; Ratel-Ramond, N.; Yi, X.; Roblin, P.; Frenzel, F.; Resch-Genger, U.; Eftekhari, A.; Bouchet, A.; Coudret, C.; Verelst, M.; Chen, X.;

Mauricot, R.; Roux, C. Heterogeneous Oxysulfide@Fluoride Core/Shell Nanocrystals for Upconversion-Based Nanothermometry. *ACS Nano* **2022**, *16*, 12107–12117.

(23) Abdukayum, A.; Chen, J. T.; Zhao, Q.; Yan, X. P. Functional near Infrared-Emitting Cr^{3+}/Pr^{3+} Co-Doped Zinc Gallogermanate Persistent Luminescent Nanoparticles with Superlong Afterglow for in Vivo Targeted Bioimaging. *J. Am. Chem. Soc.* **2013**, *135*, 14125–14133.

(24) Chen, X.; Liu, S.; Huang, K.; Nie, J.; Kang, R.; Tian, X.; Zhang, S.; Li, Y.; Qiu, J. Cr^{4+} Activated NIR-NIR Multi-Mode Luminescent Nanothermometer for Double Biological Windows. *Chem. Eng. J.* **2020**, *396*, 125201.

(25) Danilkin, M. I.; Vereschagina, N. Y.; Vainer, Y. G.; Kochiev, M. V.; Ambrozevich, S. A.; Romet, I.; Mändar, H.; Morozov, A. N.; Repeev, Y. A.; Spassky, D. A.; Shutov, A. V.; Seleznev, L. V.; Mokrousova, D. V.; Selyukov, A. S. Ultrafast and Slow Mn^{2+} Luminescence in Lithium Tetraborate. *J. Alloys Compd.* **2021**, *883*, 160852.

(26) Marciniak, L.; Trejgis, K. Luminescence Lifetime Thermometry with Mn^{3+}-Mn^{4+} Co-Doped Nanocrystals. *J. Mater. Chem. C* **2018**, *6*, 7092–7100.

(27) Wang, Z.; Ji, H.; Xu, J.; Hou, X.; Ueda, J.; Tanabe, S.; Yi, S.; Zhou, Y.; Chen, D. Microsized Red Luminescent $MgAl_2O_4$:Mn^{4+} Single-Crystal Phosphor Grown in Molten Salt for White LEDs. *Inorg. Chem.* **2020**, *59*, 18374–18383.

(28) Marciniak, L.; Kniec, K.; Elżbieciak-Piecka, K.; Trejgis, K.; Stefanska, J.; Dramićanin, M. Luminescence Thermometry with Transition Metal Ions. A Review. *Coord. Chem. Rev.* **2022**, *469*, 214671.

(29) Li, H.; Wang, X.; Huang, D.; Chen, G. Recent Advances of Lanthanide-Doped Upconversion Nanoparticles for Biological Applications. *Nanotechnology* **2020**, *31*, 072001.

(30) Maturi, F. E.; Brites, C. D. S.; Silva, R. R.; Nigoghossian, K.; Wilson, D.; Ferreira, R. A. S.; Ribeiro, S. J. L.; Carlos, L. D. Sustainable Smart Tags with Two-Step Verification for Anticounterfeiting Triggered by the Photothermal Response of Upconverting Nanoparticles. *Adv. Photonics Res.* **2022**, *3*, 2100227.

(31) Liu, Y.; Wei, Z.; Liao, X.; Zhou, J. Multichannel Lanthanide-Doped Nanoprobes Improve Diagnostic Performance. *Accounts Mater. Res.* **2020**, *1*, 225–235.

(32) Wang, J.; Ma, Q.; Wang, Y.; Shen, H.; Yuan, Q. Recent Progress in Biomedical Applications of Persistent Luminescence Nanoparticles. *Nanoscale* **2017**, 9, 6204–6218.

(33) Zhuo, Y.; Brgoch, J. Opportunities for Next-Generation Luminescent Materials through Artificial Intelligence. *J. Phys. Chem. Lett.* **2021**, *12*, 764–772.

(34) Algar, W. R.; Massey, M.; Rees, K.; Higgins, R.; Krause, K. D.; Darwish, G. H.; Peveler, W. J.; Xiao, Z.; Tsai, H. Y.; Gupta, R.; Lix, K.; Tran, M. V.; Kim, H. Photoluminescent Nanoparticles for Chemical and Biological Analysis and Imaging. *Chem. Rev*. **2021**, *121*, 9243–9358.

(35) Kobayashi, H.; Ogawa, M.; Alford, R.; Choyke, P. L.; Urano, Y. New Strategies for Fluorescent Probe Design in Medical Diagnostic Imaging. *Chem. Rev.* **2010**, *110*, 2620–2640.

(36) Mérian, J.; Gravier, J.; Navarro, F.; Texier, I. Fluorescent Nanoprobes Dedicated to in Vivo Imaging: From Preclinical Validations to Clinical Translation. *Molecules* **2012**, *17*, 5564–5591.

(37) Shen, Q.; Wang, S.; Yang, N. Di; Zhang, C.; Wu, Q.; Yu, C. Recent Development of Small-Molecule Organic Fluorophores for Multifunctional Bioimaging in the Second near-Infrared Window. *J. Lumin.* **2020**, *225*, 117338.

(38) He, S.; Song, J.; Qu, J.; Cheng, Z. Crucial Breakthrough of Second Near-Infrared Biological Window Fluorophores: Design and Synthesis toward Multimodal Imaging and Theranostics. *Chem. Soc. Rev.* **2018**,*47,* 4258–4278.

(39) Hemmer, E.; Venkatachalam, N.; Hyodo, H.; Hattori, A.; Ebina, Y.; Kishimoto, H.; Soga, K. Upconverting and NIR Emitting Rare Earth Based Nanostructures for NIR-Bioimaging. *Nanoscale* **2013**, *5*, 11339–11361.

(40) Golovynskyi, S.; Golovynska, I.; Stepanova, L. I.; Datsenko, O. I.; Liu, L.; Qu, J.; Ohulchanskyy, T. Y. Optical Windows for Head Tissues in Near-Infrared and Short-Wave Infrared Regions: Approaching Transcranial Light Applications. *J. Biophotonics* **2018**, *11*, e201800141.

(41) Hemmer, E.; Benayas, A.; Légaré, F.; Vetrone, F. Exploiting the Biological Windows: Current Perspectives on Fluorescent Bioprobes Emitting above 1000 Nm. *Nanoscale Horiz.* **2016**, *1*, 168–184.

(42) Kenry; Duan, Y.; Liu, B. Recent Advances of Optical Imaging in the Second Near-Infrared Window. *Adv. Mater.* **2018**, *30*, 1802394.

(43) Shi, J.; Sun, X.; Zheng, S.; Song, L.; Zhang, F.; Madl, T.; Zhang, Y.; Zhang, H.; Hong, M. Tin-Doped Near-Infrared Persistent Luminescence Nanoparticles with Considerable Improvement of Biological Window Activation for Deep Tumor Photodynamic Therapy. *ACS Appl. Bio Mater.* **2020**, *3*, 5995–6004.

(44) Wu, C.; Wu, Y.; Zhu, X.; Zhang, J.; Liu, J.; Zhang, Y. Near-Infrared-Responsive Functional Nanomaterials: The First Domino of Combined Tumor Therapy. *Nano Today* **2021**, *36*, 100963.

(45) Lingeshwar Reddy, K.; Balaji, R.; Kumar, A.; Krishnan, V. Lanthanide Doped Near Infrared Active Upconversion Nanophosphors: Fundamental Concepts, Synthesis Strategies, and Technological Applications. *Small* **2018**, *14*, 1801304.

(46) Xia, Q.; Chen, Z.; Yu, Z.; Wang, L.; Qu, J.; Liu, R. Aggregation-Induced Emission-Active Near-Infrared Fluorescent Organic Nanoparticles for Noninvasive Long-Term Monitoring of Tumor Growth. *ACS Appl. Mater. Interfaces* **2018**, *10*, 17081–17088.

(47) Shi, B.; Jie, K.; Zhou, Y.; Zhou, J.; Xia, D.; Huang, F. Nanoparticles with Near-Infrared Emission Enhanced by Pillararene-Based Molecular Recognition in Water. *J. Am. Chem. Soc.* **2016**, *138*, 80–83.

(48) Jackson, C. T.; Jeong, S.; Dorlhiac, G. F.; Landry, M. P. Advances in Engineering Near-Infrared Luminescent Materials. *iScience* **2021**, *24*, 102156.

(49) Santos, O.; Cancino-Bernardi, J.; Pincela Lins, P. M.; Sampaio, D.; Pavan, T.; Zucolotto, V. Near-Infrared Photoactive Theragnostic Gold Nanoflowers for Photoacoustic Imaging and Hyperthermia. *ACS Appl. Bio Mater.* **2021**, *4*, 6780–6790.

(50) Liu, T. M.; Conde, J.; Lipiński, T.; Bednarkiewicz, A.; Huang, C. C. Revisiting the Classification of NIR-Absorbing/Emitting Nanomaterials for in Vivo Bioapplications. *NPG Asia Mater*. **2016**, 8, e295.

(51) Ai, T.; Shang, W.; Yan, H.; Zeng, C.; Wang, K.; Gao, Y.; Guan, T.; Fang, C.; Tian, J. Near Infrared-Emitting Persistent Luminescent Nanoparticles for Hepatocellular Carcinoma Imaging and Luminescence-Guided Surgery. *Biomaterials* **2018**, *167*, 216–225.

(52) Mini Krishna, K.; Jayaraj, M. K. Oxide Luminescent Materials. In: *Nanostructured Metal Oxides and Devices. Materials Horizons: From Nature to Nanomaterials. Springer* **2020**, 1–46.

(53) Cotton, S. Lanthanide and Actinide Chemistry. W*iley*, **2006**.

(54) Zheng, B.; Fan, J.; Chen, B.; Qin, X.; Wang, J.; Wang, F.; Deng, R.; Liu, X. Rare-Earth Doping in Nanostructured Inorganic Materials. *Chem. Rev.* 2022, 122, 5519–5603.

(55) Chen, X.; Liu, Y.; Tu, D. A General Introduction to Lanthanide Ions. In*: Lanthanide-Doped Luminescent Nanomaterials. Nanomedicine and Nanotoxicology. Springer* **2014**, 1–16.

(56) Bünzli, J.-C. G.; Eliseeva, S. V. Basics of Lanthanide Photophysics. In: *Lanthanide Luminescence. Springer Series on Fluorescence. Springer* **2010**, *7*, 1–46.

(57) Russell, H. N.; Saunders, F. A. New Regularities in the Spectra of the Alkaline Earths. *Astrophys. J.* **1925**, *61*, 38.

(58) McDaniel, D. H. Spin Factoring as an Aid in the Determination of Spectroscopic Terms. *J. Chem. Educ.* **1977**, *54*, 147.

(59) Xu, R.; Dai, Z. Alternative Mathematical Technique to Determine LS Spectral Terms. *J. Phys. B: At. Mol. Opt. Phys.* **2006**, *39*, 3221.

(60) Bünzli, J. C. G. Lanthanide Luminescence for Biomedical Analyses and Imaging. *Chem. Rev.* **2010**, *110*, 2729–2755.

(61) Eliseeva, S. V.; Bünzli, J. C. G. Lanthanide Luminescence for Functional Materials and Bio-Sciences. *Chem. Soc. Rev.* **2010**, *39*, 189–227.

(62) Jia, T.; Chen, G. Lanthanide Nanoparticles for Near-Infrared II Theranostics. *Coord. Chem. Rev.* **2022**, *471*, 214724.

(63) Song, Y.; Sun, R.; Sun, G.; Xie, Y.; Sun, L. Upconversion/Downshifting

Multimode Luminescence of Lanthanide-Doped Nanocrystals for Multidimensional Information Encoding Security. *Chem. Asian J.* **2022**, 17, e202200537.

(64) Huang, X. Realizing Efficient Upconversion and Down-Shifting Dual-Mode Luminescence in Lanthanide-Doped $NaGdF_4$ Core-Shell-Shell Nanoparticles through Gadolinium Sublattice-Mediated Energy Migration. *Dyes Pigm.* **2016**, *130*, 99–105.

(65) Sun, G.; Xie, Y.; Sun, L.; Zhang, H. Lanthanide Upconversion and Downshifting Luminescence for Biomolecules Detection. *Nanoscale Horiz.* **2021**, *6*, 766–780.

(66) Datt, R.; Bishnoi, S.; Lee, H. K. H.; Arya, S.; Gupta, S.; Gupta, V.; Tsoi, W. C. Down-conversion Materials for Organic Solar Cells: Progress, Challenges, and Perspectives. *Aggregate* **2022**, *3*, e185.

(67) Wang, M.; Abbineni, G.; Clevenger, A.; Mao, C.; Xu, S. Upconversion Nanoparticles: Synthesis, Surface Modification and Biological Applications. *Nanomedicine* **2011**, *7*, 710–729.

(68) Shalav, A.; Richards, B. S.; Green, M. A. Luminescent Layers for Enhanced Silicon Solar Cell Performance: Up-Conversion. *Sol. Energy Mater. Sol. Cells* **2007**, *91*, 829–842.

(69) Singh, P.; Singh, P.; Singh, S. K. Photon Upconversion Spectroscopy. In: *Modern Techniques of Spectroscopy. Progress in Optical Science and Photonics. Springer* **2021**, *13*, 389–407.

(70) Chen, G.; Qiu, H.; Prasad, P. N.; Chen, X. Upconversion Nanoparticles: Design, Nanochemistry, and Applications in Theranostics. *Chem. Rev.* **2014**, *114*, 5161–5214.

(71) Du, K.; Feng, J.; Gao, X.; Zhang, H. Nanocomposites Based on Lanthanide-Doped Upconversion Nanoparticles: Diverse Designs and Applications. *Light Sci Appl.* **2022**, *11*, 222.

(72) Li, D.; Ågren, H.; Chen, G. Near Infrared Harvesting Dye-Sensitized Solar Cells Enabled by Rare-Earth Upconversion Materials. *Dalton Trans.* **2018**, *47*, 8526–8537.

(73) Lei, P.; Feng, J.; Zhang, H. Emerging Biomaterials: Taking Full Advantage of the Intrinsic Properties of Rare Earth Elements. *Nano Today* **2020**, *35*, 100952.

(74) Dong, H.; Sun, L. D.; Yan, C. H. Energy Transfer in Lanthanide Upconversion Studies for Extended Optical Applications. *Chem. Soc. Rev.* **2015**, *44*, 1608–1634.

(75) Wang, X.; Yan, L.; Liu, S.; Zhang, P.; Huang, R.; Zhou, B. Enhancing Energy Migration Upconversion through a Migratory Interlayer in the Core-Shell-Shell Nanostructure towards Latent Fingerprinting. *Nanoscale* **2020**, *12*, 18807–18814.

(76) Su, Q.; Han, S.; Xie, X.; Zhu, H.; Chen, H.; Chen, C. K.; Liu, R. S.; Chen, X.;

Wang, F.; Liu, X. The Effect of Surface Coating on Energy Migration-Mediated Upconversion. *J. Am. Chem. Soc.* **2012**, *134*, 20849–20857.

(77) Han, S.; Qin, X.; An, Z.; Zhu, Y.; Liang, L.; Han, Y.; Huang, W.; Liu, X. Multicolour Synthesis in Lanthanide-Doped Nanocrystals through Cation Exchange in Water. *Nat. Commun.* **2016**, *7*, 13059.

(78) Chen, X.; Jin, L.; Sun, T.; Kong, W.; Yu, S. F.; Wang, F. Energy Migration Upconversion in Ce(III)-Doped Heterogeneous Core−Shell−Shell Nanoparticles. *Small* **2017**, *13*, 1701479.

(79) Wang, F.; Deng, R.; Wang, J.; Wang, Q.; Han, Y.; Zhu, H.; Chen, X.; Liu, X. Tuning Upconversion through Energy Migration in Core-Shell Nanoparticles. *Nat. Mater.* **2011**, *10*, 968–973.

(80) Zhu, Q.; Sun, T.; Chung, M. N.; Sun, X.; Xiao, Y.; Qiao, X.; Wang, F. Yb^{3+}-Sensitized Upconversion and Downshifting Luminescence in Nd^{3+} Ions through Energy Migration. *Dalt. Trans.* **2018**, *47*, 8581–8584.

(81) Wen, S.; Zhou, J.; Zheng, K.; Bednarkiewicz, A.; Liu, X.; Jin, D. Advances in Highly Doped Upconversion Nanoparticles. *Nat. Commun.* **2018**, *9*, 2415.

(82) Zheng, K.; Han, S.; Zeng, X.; Wu, Y.; Song, S.; Zhang, H.; Liu, X. Rewritable Optical Memory Through High-Registry Orthogonal Upconversion. *Adv. Mater.* **2018**, *30*, 1801726.

(83) Yi, Z.; Luo, Z.; Qin, X.; Chen, Q.; Liu, X. Lanthanide-Activated Nanoparticles: A Toolbox for Bioimaging, Therapeutics, and Neuromodulation. *Acc. Chem. Res.* **2020**, *53*, 2692–2704.

(84) Han, S.; Deng, R.; Xie, X.; Liu, X. Enhancing Luminescence in Lanthanide-Doped Upconversion Nanoparticles. *Angew. Chem. Int. Ed.* **2014**, *53*, 11702–11715.

(85) Krämer, K. W.; Biner, D.; Frei, G.; Güdel, H. U.; Hehlen, M. P.; Lüthi, S. R. Hexagonal Sodium Yttrium Fluoride Based Green and Blue Emitting Upconversion Phosphors. *Chem. Mater.* **2004**, *16*, 1244–1251.

(86) Tessitore, G.; Mandl, G. A.; Brik, M. G.; Park, W.; Capobianco, J. A. Recent Insights into Upconverting Nanoparticles: Spectroscopy, Modeling, and Routes to Improved Luminescence. *Nanoscale* **2019**, *11*, 12015–12029.

(87) Shi, R.; Mudring, A.-V. Phonon-Mediated Nonradiative Relaxation in Ln^{3+}-Doped Luminescent Nanocrystals. ACS Materials Lett. **2022**, *18*, 1882–1903.

(88) Riseberg, L. A.; Weber, M. J. Relaxation Phenomena in Rare-Earth Luminescence. *Prog. Opt.* **1977**, *14*, 89–159.

(89) DaCosta, M. V.; Doughan, S.; Han, Y.; Krull, U. J. Lanthanide Upconversion Nanoparticles and Applications in Bioassays and Bioimaging: A Review. *Anal. Chim. Acta.* **2014**, *832*, 1–33.

(90) Zhou, J.; Liu, Q.; Feng, W.; Sun, Y.; Li, F. Upconversion Luminescent Materials: Advances and Applications. *Chem. Rev.* **2015**, *115*, 395–465.

(91) Egger, P.; Rogin, P.; Riedener, T.; Güdel, H. U.; Wickleder, M. S.; Hulliger, J. Ba_2ErCl_7 - A New near IR to near UV Upconversion Material. *Adv. Mater.* **1996**, *8*, 668–672.

(92) Chen, J.; Zhao, J. X. Upconversion Nanomaterials: Synthesis, Mechanism, and Applications in Sensing. *Sensors* **2012**, 12, 2414–2435.

(93) Shan, J.; Kong, W.; Wei, R.; Yao, N.; Ju, Y. An Investigation of the Thermal Sensitivity and Stability of the β-$NaYF_4$:Yb,Er Upconversion Nanophosphors. *J. Appl. Phys.* **2010**, *107*, 054901.

(94) Lei, Y.; Song, H.; Yang, L. Upconversion Luminescence, Intensity Saturation Effect, and Thermal Effect in Gd_2O_3:Er^3,Yb^{3+} Nanowires. *J. Chem. Phys.* **2005**, *123*, 174710.

(95) Haase, M.; Schäfer, H.; Schäfer, H.; Haase, M. Upconverting Nanoparticles. *Angew. Chem. Int. Ed.* **2011**, *50*, 5808–5829.

(96) Liu, Y.; Meng, X.; Bu, W. Upconversion-Based Photodynamic Cancer Therapy. *Coord. Chem. Rev.* **2019**, *379*, 82–98.

(97) Runowski, M.; Stopikowska, N.; Szeremeta, D.; Goderski, S.; Skwierczyńska, M. S.; Lis, S. Upconverting Lanthanide Fluoride Core@Shell Nanorods for Luminescent Thermometry in the First and Second Biological Windows: β-$NaYF_4$:Yb^{3+}−Er^{3+}@SiO_2 Temperature Sensor. *ACS Appl. Mater. Interfaces* **2019**, *11*, 13389–13396.

(98) Thoma, R. E.; Insley, H.; Hebert, G. M. The Sodium Fluoride-Lanthanide Trifluoride Systems. *Inorg. Chem.* **1966**, *5*, 1222–1229.

(99) Mai, H. X.; Zhang, Y. W.; Si, R.; Yan, Z. G.; Sun, L. D.; You, L. P.; Yan, C. H. High-Quality Sodium Rare-Earth Fluoride Nanocrystals: Controlled Synthesis and Optical Properties. *J. Am. Chem. Soc.* **2006**, *128*, 6426–6436.

(100) Saha, S.; Pala, R. G. S.; Sivakumar, S. Catalyzing Cubic-to-Hexagonal Phase Transition in $NaYF_4$ via Ligand Enhanced Surface Ordering. *Cryst. Growth Des.* **2018**, *18*, 5080–5088.

(101) Leménager, G.; Tusseau-Nenez, S.; Thiriet, M.; Coulon, P.-E.; Lahlil, K.; Larquet, E.; Gacoin, T. $NaYF_4$ Microstructure, beyond Their Well-Shaped Morphology. *Nanomaterials* **2019**, *9*, 1560.

(102) Szefczyk, B.; Roszak, R.; Roszak, S. Structure of the Hexagonal $NaYF_4$ Phase from First-Principles Molecular Dynamics. *RSC Adv.* **2014**, *4*, 22526–22535.

(103) Dinic, I. Z.; Mancic, L. T.; Rabanal, M. E.; Yamamoto, K.; Ohara, S.; Tamura, S.; Koji, T.; Costa, A. M. L. M.; Marinkovic, B. A.; Milosevic, O. B. Compositional and Structural Dependence of Up-Converting Rare Earth Fluorides Obtained through EDTA Assisted Hydro/Solvothermal Synthesis. *Adv. Powder Technol.* **2017**, *28*, 73–82.

(104) Karbowiak, M.; Cichos, J.; Rudowicz, C. Spectroscopic Determination of Site Symmetry and Space Group in Lanthanide-Doped Crystals: Resolving Intricate Symmetry Aspects for β-$NaLnF_4$. *Polyhedron* **2016**, *105*, 42–48.

(105) Ullah, S.; Hazra, C.; Ferreira-Neto, E. P.; Silva, T. C.; Rodrigues-Filho, U. P.; Ribeiro, S. J. L. Microwave-Assisted Synthesis of $NaYF_4:Yb^{3+}/Tm^{3+}$ Upconversion Particles with Tailored Morphology and Phase for the Design of UV/NIR-Active $NaYF_4:Yb^{3+}/Tm^{3+}@TiO_2$ Core@shell Photocatalysts. *CrystEngComm* **2017**, *19*, 3465–3475.

(106) Liu, D.; Jing, Y.; Wang, K.; Wang, Y.; Luo, G. Reaction Study of α-Phase $NaYF_4$:Yb,Er Generation via a Tubular Microreactor: Discovery of an Efficient Synthesis Strategy. *Nanoscale* **2019**, *11*, 8363–8371.

(107) Liu, S.; De, G.; Xu, Y.; Wang, X.; Liu, Y.; Cheng, C.; Wang, J. Size, Phase-Controlled Synthesis, the Nucleation and Growth Mechanisms of $NaYF_4$:Yb/Er Nanocrystals. *J. Rare Earths* **2018**, *36*, 1060–1066.

(108) Liu, L.; Zhang, D.; Zhang, Y.; Bao, Z.; Chen, L. Room Temperature Synthesis and Formation Process of α-NaYF 4 Nanocubes. *J. Mater. Sci.* **2013**, *48*, 876–883.

(109) Ding, M.; Chen, D.; Yin, S.; Ji, Z.; Zhong, J.; Ni, Y.; Lu, C.; Xu, Z. Simultaneous Morphology Manipulation and Upconversion Luminescence Enhancement of β-$NaYF_4:Yb^{3+}/Er^{3+}$ Microcrystals by Simply Tuning the KF Dosage. *Sci. Rep.* **2015**, *5*, 12745.

(110) Calil, M. A.; Melo, Á. A.; Rodrigues, E. M.; Sigoli, F. A.; Rodrigues, M. O. The Effect of Hydrothermal Treatment on the Morphologies and Optical Properties of Upconversion $NaYF_4:Ln^{3+}$ Crystals. *J. Braz. Chem. Soc.* **2017**, *28*, 1816–1821.

(111) Janjua, R. A.; Iqbal, O.; Ahmed, M. A.; Al-Kahtani, A. A.; Saeed, S.; Imran, M.; Wattoo, A. G. Homo-Hetero/Core-Shell Structure Design Strategy of $NaYF_4$ nanocrystals for Superior Upconversion Luminescence. *RSC Adv.* **2021**, *11*, 20746–20751.

(112) Chen, B.; Wang, F. Recent Advances in the Synthesis and Application of Yb-Based Fluoride Upconversion Nanoparticles. I*norg. Chem. Front.* **2020**, *7*, 1067–1081.

(113) Runowski, M.; Goderski, S.; Przybylska, D.; Grzyb, T.; Lis, S.; Martín, I. R. $Sr_2LuF_7:Yb^{3+}$-Ho^{3+}-Er^{3+} Upconverting Nanoparticles as Luminescent Thermometers in the First, Second, and Third Biological Windows. *ACS Appl. Nano Mater.* **2020**, *3*, 6406–6415.

(114) Suyver, J. F.; Grimm, J.; Van Veen, M. K.; Biner, D.; Krämer, K. W.; Güdel, H. U. Upconversion Spectroscopy and Properties of $NaYF_4$ Doped with Er^{3+}, Tm^{3+} and/or Yb^{3+}. *J. Lumin.* **2006**, *117*, 1–12.

(115) Zhou, B.; Tang, B.; Zhang, C.; Qin, C.; Gu, Z.; Ma, Y.; Zhai, T.; Yao, J. Enhancing Multiphoton Upconversion through Interfacial Energy Transfer in Multilayered Nanoparticles. *Nat. Commun.* **2020**, *11*, 1174.

(116) Shyichuk, A.; Câmara, S. S.; Weber, I. T.; Carneiro Neto, A. N.; Nunes, L. A. O.; Lis, S.; Longo, R. L.; Malta, O. L. Energy Transfer Upconversion Dynamics in $YVO_4:Yb^{3+},Er^{3+}$. *J. Lumin.* **2016**, *170*, 560–570.

(117) Wu, Q.; Xu, Z.; Wageh, S.; Al-Ghamdi, A.; Zhao, S. The Dynamic Variation of

Upconversion Luminescence Dependent on Shell Yb^{3+} Contents in $NaYF_4$: Yb^{3+},Tm^{3+}@$NaYF_4$:Yb^{3+},Er^{3+} Nanoparticles. *J. Alloys Compd.* **2022**, *891*. 162067.

(118) Rafiei Miandashti, A.; Kordesch, M. E.; Richardson, H. H. Effect of Temperature and Gold Nanoparticle Interaction on the Lifetime and Luminescence of $NaYF_4$:Yb^{3+}:Er^{3+} Upconverting Nanoparticles. *ACS Photonics* **2017**, *4*, 1864–1869.

(119) Gonçalves, I.M; Pessoa, A. R.; Hazra, C.; Correales, Y. S.; Ribeiro, S. J. L.; Menezes, L. S. Phonon-assisted NIR-to-visible upconversion in single β-$NaYF_4$ microcrystals codoped with Er^{3+} and Yb^{3+} for microthermometry applications: Experiment and theory. *J. Lumin.* **2021**, *231*, 117801.

(120) Zhao, J.; Lu, Z.; Yin, Y.; McRae, C.; Piper, J. A.; Dawes, J. M.; Jin, D.; Goldys, E. M. Upconversion Luminescence with Tunable Lifetime in $NaYF_4$:Yb,Er Nanocrystals: Role of Nanocrystal Size. *Nanoscale* **2013**, *5*, 944–952.

(121) Yu, W.; Xu, W.; Song, H.; Zhang, S. Temperature-Dependent Upconversion Luminescence and Dynamics of $NaYF_4$:Yb^{3+}/Er^{3+} nanocrystals: Influence of Particle Size and Crystalline Phase. *J. Chem. Soc. Dalt. Trans.* **2014**, *43*, 6139–6147.

(122) Ullah, S.; Ferreira-Neto, E. P.; Hazra, C.; Parveen, R.; Rojas-Mantilla, H. D.; Calegaro, M. L.; Serge-Correales, Y. E.; Rodrigues-Filho, U. P.; Ribeiro, S. J. L. Broad Spectrum Photocatalytic System Based on $BiVO_4$ and $NaYbF_4$:Tm^{3+} Upconversion Particles for Environmental Remediation under UV-Vis-NIR Illumination. *Appl. Catal. B Environ.* **2019**, *243*, 121–135.

(123) Wang, G.; Qin, W.; Zhang, J.; Wang, L.; Wei, G.; Zhu, P.; Kim, R. Controlled Synthesis and Luminescence Properties from Cubic to Hexagonal $NaYF_4$:Ln^{3+} (Ln = Eu and Yb/Tm) Microcrystals. *J. Alloys Compd.* **2009**, *475*, 452–455.

(124) De, G.; Qin, W.; Zhang, J.; Zhang, J.; Wang, Y.; Cao, C.; Cui, Y. Infrared-to-Ultraviolet up-Conversion Luminescence of YF_3:Yb^{3+},Tm^{3+} Microsheets. *J. Lumin.* **2007**, *122–123*, 128–130.

(125) Wang, Z.; Meijerink, A. Concentration Quenching in Upconversion Nanocrystals. *J. Phys. Chem. C* **2018**, *122*, 26298–26306.

(126) Rabouw, F. T.; Prins, P. T.; Villanueva-Delgado, P.; Castelijns, M.; Geitenbeek, R. G.; Meijerink, A. Quenching Pathways in $NaYF_4$:Er^{3+},Yb^{3+} Upconversion Nanocrystals. *ACS Nano* **2018**, *12*, 4812–4823.

(127) Chen, X.; Jin, L.; Kong, W.; Sun, T.; Zhang, W.; Liu, X.; Fan, J.; Yu, S. F.; Wang, F. Confining Energy Migration in Upconversion Nanoparticles towards Deep Ultraviolet Lasing. *Nat. Commun.* **2016**, *7*, 10304.

(128) Chen, B.; Wang, F. Combating Concentration Quenching in Upconversion Nanoparticles. *Acc. Chem. Res.* **2020**, *53*, 358–367.

(129) Ge, X.; Liu, J.; Sun, L. Controlled Optical Characteristics of Lanthanide Doped Upconversion Nanoparticles for Emerging Applications. *Dalton Trans.* **2017**, *46*, 16729–16737.

(130) Chien, H. W.; Wu, C. H.; Yang, C. H.; Wang, T. L. Multiple Doping Effect of $LiYF_4:Yb^{3+}/Er^{3+}/Ho^{3+}/Tm^{3+}@LiYF_4:Yb^{3+}$ Core/Shell Nanoparticles and Its Application in Hg^{2+} Sensing Detection. *J. Alloys Compd.* **2019**, *806*, 272–282.

(131) Huang, X. Synthesis, Multicolour Tuning, and Emission Enhancement of Ultrasmall $LaF_3:Yb^{3+}/Ln^{3+}$ (Ln = Er, Tm, and Ho) Upconversion Nanoparticles. *J. Mater. Sci.* **2016**, *51*, 3490–3499.

(132) Zhang, Y.; Chen, B.; Xu, S.; Li, X.; Zhang, J.; Sun, J.; Zheng, H.; Tong, L.; Sui, G.; Zhong, H.; Xia, H.; Hua, R. Dually Functioned Core-Shell $NaYF_4:Er^{3+}/Yb^{3+}@NaYF_4:Tm^{3+}/Yb^{3+}$ Nanoparticles as Nano-Calorifiers and Nano-Thermometers for Advanced Photothermal Therapy. *Sci. Rep.* **2017**, *7*, . 11849.

(133) Wang, F.; Wang, J.; Liu, X. Direct Evidence of a Surface Quenching Effect on Size-Dependent Luminescence of Upconversion Nanoparticles. *Angew. Chemie - Int. Ed.* **2010**, *49*, 7456–7460.

(134) Shen, B.; Cheng, S.; Gu, Y.; Ni, D.; Gao, Y.; Su, Q.; Feng, W.; Li, F. Revisiting the Optimized Doping Ratio in Core/Shell Nanostructured Upconversion Particles. *Nanoscale* **2017**, *9*, 1964–1971.

(135) Fan, Y.; Liu, L.; Zhang, F. Exploiting Lanthanide-Doped Upconversion Nanoparticles with Core/Shell Structures. *Nano Today* **2019**, *25*, 68–84.

(136) Wang, Y. F.; Liu, G. Y.; Sun, L. D.; Xiao, J. W.; Zhou, J. C.; Yan, C. H. Nd^{3+}-Sensitized Upconversion Nanophosphors: Efficient in Vivo Bioimaging Probes with Minimized Heating Effect. *ACS Nano* **2013**, *7*, 7200–7206.

(137) Lu, F.; Yang, L.; Ding, Y.; Zhu, J. J. Highly Emissive Nd^{3+}-Sensitized Multilayered Upconversion Nanoparticles for Efficient 795 nm Operated Photodynamic Therapy. *Adv. Funct. Mater.* **2016**, *26*, 4778–4785.

(138) Hao, S.; Chen, G.; Yang, C.; Shao, W.; Wei, W.; Liu, Y.; Prasad, P. N. Nd^{3+}-Sensitized Multicolor Upconversion Luminescence from a Sandwiched Core/Shell/Shell Nanostructure. *Nanoscale* **2017**, *9*, 10633–10638 .

(139) Wiesholler, L. M.; Frenzel, F.; Grauel, B.; Würth, C.; Resch-Genger, U.; Hirsch, T. Yb,Nd,Er-Doped Upconversion Nanoparticles: 980 nm: Versus 808 nm Excitation. *Nanoscale* **2019**, *11*, 13440–13449.

(140) Ding, X.; Liu, J.; Liu, D.; Li, J.; Wang, F.; Li, L.; Wang, Y.; Song, S.; Zhang, H. Multifunctional Core/Satellite Polydopamine@Nd^{3+}-Sensitized Upconversion Nanocomposite: A Single 808 nm near-Infrared Light-Triggered Theranostic Platform for in Vivo Imaging-Guided Photothermal Therapy. *Nano Res.* **2017**, *10*, 3434–3446.

(141) Xie, X.; Gao, N.; Deng, R.; Sun, Q.; Xu, Q. H.; Liu, X. Mechanistic Investigation of Photon Upconversion in Nd^{3+}- Sensitized Core-Shell Nanoparticles. *J. Am. Chem. Soc.* **2013**, *135*, 12608–12611.

(142) Wang, D.; Xue, B.; Kong, X.; Tu, L.; Liu, X.; Zhang, Y.; Chang, Y.; Luo, Y.; Zhao, H.; Zhang, H. 808 nm Driven Nd^{3+}-Sensitized Upconversion Nanostructures for Photodynamic Therapy and Simultaneous Fluorescence Imaging. *Nanoscale*

2015, *7*, 190–197.

(143) Chen, X.; Tang, Y.; Liu, A.; Zhu, Y.; Gao, D.; Yang, Y.; Sun, J.; Fan, H.; Zhang, X. NIR-to-Red Upconversion Nanoparticles with Minimized Heating Effect for Synchronous Multidrug Resistance Tumor Imaging and Therapy. *ACS Appl. Mater. Interfaces* **2018**, *10*, 14378–14388.

(144) Wang, F.; Han, Y.; Lim, C. S.; Lu, Y.; Wang, J.; Xu, J.; Chen, H.; Zhang, C.; Hong, M.; Liu, X. Simultaneous Phase and Size Control of Upconversion Nanocrystals through Lanthanide Doping. *Nature* **2010**, *463*, 1061–1065.

(145) Wang, X.; Zhuang, J.; Peng, Q.; Li, Y. A General Strategy for Nanocrystal Synthesis. *Nature* **2005**, *437*, 121–124.

(146) Boyer, J. C.; Vetrone, F.; Cuccia, L. A.; Capobianco, J. A. Synthesis of Colloidal Upconverting $NaYF_4$ Nanocrystals Doped with Er^{3+}, Yb^{3+} and Tm^{3+}, Yb^{3+} via Thermal Decomposition of Lanthanide Trifluoroacetate Precursors. *J. Am. Chem. Soc.* **2006**, *128*, 7444–7445.

(147) Chen, B.; Kong, W.; Wang, N.; Zhu, G.; Wang, F. Oleylamine-Mediated Synthesis of Small $NaYbF_4$ Nanoparticles with Tunable Size. *Chem. Mater.* **2019**, *31*, 4779–4786.

(148) Liu, Y.; Lu, Y.; Yang, X.; Zheng, X.; Wen, S.; Wang, F.; Vidal, X.; Zhao, J.; Liu, D.; Zhou, Z.; Ma, C.; Zhou, J.; Piper, J. A.; Xi, P.; Jin, D. Amplified Stimulated Emission in Upconversion Nanoparticles for Super-Resolution Nanoscopy. *Nature* **2017**, *543*, 229–233.

(149) Yi, G. S.; Chow, G. M. Water-Soluble $NaYF_4$:Yb,Er(Tm)/$NaYF_4$/Polymer Core/Shell/Shell Nanoparticles with Significant Enhancement of Upconversion Fluorescence. *Chem. Mater.* **2007**, *19*, 341–343.

(150) Johnson, N. J. J.; Korinek, A.; Dong, C.; Van Veggel, F. C. J. M. Self-Focusing by Ostwald Ripening: A Strategy for Layer-by-Layer Epitaxial Growth on Upconverting Nanocrystals. *J. Am. Chem. Soc.* **2012**, *134*, 11068–11071.

(151) Wang, F.; Deng, R.; Liu, X. Preparation of Core-Shell $NaGdF_4$ Nanoparticles Doped with Luminescent Lanthanide Ions to be Used as Upconversion-Based Probes. *Nat. Protoc.* **2014**, *9*, 1634–1644.

(152) De Camillis, S.; Ren, P.; Cao, Y.; Plöschner, M.; Denkova, D.; Zheng, X.; Lu, Y.; Piper, J. A. Controlling the Non-Linear Emission of Upconversion Nanoparticles to Enhance Super-Resolution Imaging Performance. *Nanoscale* **2020**, *12*, 20347–20355.

(153) Shi, R.; Ling, X.; Li, X.; Zhang, L.; Lu, M.; Xie, X.; Huang, L.; Huang, W. Tuning Hexagonal $NaYbF_4$ Nanocrystals down to Sub-10 nm for Enhanced Photon Upconversion. *Nanoscale* **2017**, *9*, 13739–13746.

(154) Ye, S.; Xiao, P.; Liao, H.; Li, S.; Wang, D. Fast Synthesis of Sub-10 nm β-$NaYF_4$:Yb^{3+}, Er^{3+}@$NaYF_4$ Core-Shell Upconversion Nanocrystals Mediated by Oleate Ligands. *Mater. Res. Bull.* **2018**, *103*, 279–284.

(155) Jia, X.; Yin, J.; He, D.; He, X.; Wang, K.; Chen, M.; Li, Y. Polyacrylic Acid

Modified Upconversion Nanoparticles for Simultaneous PH-Triggered Drug Delivery and Release Imaging. *J. Biomed. Nanotechnol.* **2013**, *9*, 2063–2072.

(156) Wilhelm, S.; Kaiser, M.; Würth, C.; Heiland, J.; Carrillo-Carrion, C.; Muhr, V.; Wolfbeis, O. S.; Parak, W. J.; Resch-Genger, U.; Hirsch, T. Water Dispersible Upconverting Nanoparticles: Effects of Surface Modification on Their Luminescence and Colloidal Stability. *Nanoscale* **2015**, *7*, 1403–1410.

(157) Dong, A.; Ye, X.; Chen, J.; Kang, Y.; Gordon, T.; Kikkawa, J. M.; Murray, C. B. A Generalized Ligand-Exchange Strategy Enabling Sequential Surface Functionalization of Colloidal Nanocrystals. *J. Am. Chem. Soc.* **2011**, *133*, 998–1006.

(158) Bastos, V.; Oskoei, P.; Andresen, E.; Saleh, M. I.; Rühle, B.; Resch-Genger, U.; Oliveira, H. Stability, Dissolution, and Cytotoxicity of $NaYF_4$-Upconversion Nanoparticles with Different Coatings. *Sci. Rep.* **2022**, *12*, 3770.

(159) Gee, A.; Xu, X. Surface Functionalisation of Upconversion Nanoparticles with Different Moieties for Biomedical Applications. *Surfaces* **2018**, *1*, 96–121.

(160) Muhr, V.; Wilhelm, S.; Hirsch, T.; Wolfbeis, O. S. Upconversion Nanoparticles: From Hydrophobic to Hydrophilic Surfaces. *Acc. Chem. Res.* **2014**, *47*, 3481–3493.

(161) Andresen, E.; Würth, C.; Prinz, C.; Michaelis, M.; Resch-Genger, U. Time-Resolved Luminescence Spectroscopy for Monitoring the Stability and Dissolution Behaviour of Upconverting Nanocrystals with Different Surface Coatings. *Nanoscale* **2020**, *12*, 12589–12601.

(162) Zhang, T.; Ge, J.; Hu, Y.; Yin, Y. A General Approach for Transferring Hydrophobic Nanocrystals into Water. *Nano Lett.* **2007**, *7*, 3203–3207.

(163) Himmelstoß, S. F.; Hirsch, T. Long-Term Colloidal and Chemical Stability in Aqueous Media of $NaYF_4$-Type Upconversion Nanoparticles Modified by Ligand-Exchange. *Part. Part. Syst. Charact.* **2019**, *36*, 1900235.

(164) Brites, C. D. S.; Zhuang, B.; Debasu, M. L.; Ding, D.; Qin, X.; Maturi, F. E.; Lim, W. W. Y.; Soh, D. W.; Rocha, J.; Yi, Z.; Liu, X.; Carlos, L. D. Decoding a Percolation Phase Transition of Water at ~330 K with a Nanoparticle Ruler. *J. Phys. Chem. Lett.* **2020**, *11*, 6704–6711.

(165) Hazra, C.; Skripka, A.; Ribeiro, S. J. L.; Vetrone, F. Erbium Single-Band Nanothermometry in the Third Biological Imaging Window: Potential and Limitations. *Adv. Opt. Mater.* **2020**, *8*, 2001178.

(166) Rafique, R.; Kailasa, S. K.; Park, T. J. Recent Advances of Upconversion Nanoparticles in Theranostics and Bioimaging Applications. *TrAC, Trends Anal. Chem.* **2019**, *120*, 115646.

(167) Kim, J.; Kwon, J. H.; Jang, J.; Lee, H.; Kim, S.; Hahn, Y. K.; Kim, S. K.; Lee, K. H.; Lee, S.; Pyo, H.; Song, C. S.; Lee, J. Rapid and Background-Free Detection of Avian Influenza Virus in Opaque Sample Using NIR-to-NIR Upconversion Nanoparticle-Based Lateral Flow Immunoassay Platform. *Biosens. Bioelectron.* **2018**, *112*, 209–215.

(168) Lee, G.; Park, Y. Il. Lanthanide-Doped Upconversion Nanocarriers for Drug and Gene Delivery. *Nanomaterials* **2018**, *8*, 511.

(169) Jin, F.; Qi, J.; Liu, D.; You, Y.; Shu, G.; Du, Y.; Wang, J.; Xu, X.; Ying, X.; Ji, J.; Du, Y. Cancer-Cell-Biomimetic Upconversion Nanoparticles Combining Chemo-Photodynamic Therapy and CD73 Blockade for Metastatic Triple-Negative Breast Cancer. *J. Control. Release* **2021**, *337*, 90–104.

(170) Zhou, J.; Sun, Y.; Du, X.; Xiong, L.; Hu, H.; Li, F. Dual-Modality in Vivo Imaging Using Rare-Earth Nanocrystals with near-Infrared to near-Infrared (NIR-to-NIR) Upconversion Luminescence and Magnetic Resonance Properties. *Biomaterials* **2010**, *31*, 3287–3295.

(171) Atabaev, T. S.; Molkenova, A. Upconversion Optical Nanomaterials Applied for Photocatalysis and Photovoltaics: Recent Advances and Perspectives. *Front. Mater. Sci*. **2019**, *13*, 335–341.

(172) Li, Z.; Huang, L.; Zhang, Y.; Zhao, Y.; Yang, H.; Han, G. Near-Infrared Light Activated Persistent Luminescence Nanoparticles via Upconversion. *Nano Res.* **2017**, *10*, 1840–1846.

(173) Hu, L.; Wang, P.; Zhao, M.; Liu, L.; Zhou, L.; Li, B.; Albaqami, F. H.; El-Toni, A. M.; Li, X.; Xie, Y.; Sun, X.; Zhang, F. Near-Infrared Rechargeable “Optical Battery” Implant for Irradiation-Free Photodynamic Therapy. *Biomaterials* **2018**, *163*, 154–162.

(174) Sun, S. K.; Wang, H. F.; Yan, X. P. Engineering Persistent Luminescence Nanoparticles for Biological Applications: From Biosensing/Bioimaging to Theranostics. *Acc. Chem. Res.* **2018**, *51*, 1131–1143.

(175) Huang, K.; Le, N.; Wang, J. S.; Huang, L.; Zeng, L.; Xu, W. C.; Li, Z.; Li, Y.; Han, G. Designing Next Generation of Persistent Luminescence: Recent Advances in Uniform Persistent Luminescence Nanoparticles. *Adv. Mater*. **2022**, *34*, 2107962.

(176) Maldiney, T.; Bessière, A.; Seguin, J.; Teston, E.; Sharma, S. K.; Viana, B.; Bos, A. J. J.; Dorenbos, P.; Bessodes, M.; Gourier, D.; Scherman, D.; Richard, C. The in Vivo Activation of Persistent Nanophosphors for Optical Imaging of Vascularization, Tumours and Grafted Cells. *Nat. Mater.* **2014**, *13*, 418–426.

(177) Singh, S. K. Red and Near Infrared Persistent Luminescence Nano-Probes for Bioimaging and Targeting Applications. *RSC Adv*. **2014**, *4*, 58674–58698..

(178) Rodrigues, L. C. V.; Brito, H. F.; Hölsä, J.; Stefani, R.; Felinto, M. C. F. C.; Lastusaari, M.; Laamanen, T.; Nunes, L. A. O. Discovery of the Persistent Luminescence Mechanism of $CdSiO_3$:Tb^{3+}. *J. Phys. Chem. C* **2012**, *116*, 11232–11240.

(179) Xu, J.; Tanabe, S. Persistent Luminescence Instead of Phosphorescence: History, Mechanism, and Perspective. *J. Lumin*. **2019**, *205*, 581–620.

(180) Du, J.; Poelman, D. Identifying Near-Infrared Persistent Luminescence in Cr^{3+}-Doped Magnesium Gallogermanates Featuring Afterglow Emission at Extremely Low Temperature. *Adv. Opt. Mater.* **2020**, *8*, 1901848.

(181) Arras, J.; Bräse, S. The World Needs New Colors: Cutting Edge Mobility Focusing on Long Persistent Luminescence Materials. *ChemPhotoChem* **2018**, *2*, 55–66.

(182) Cho, P.; Wood, A.; Mahalingam, K.; Eyink, K. Defect Detection in Atomic Resolution Transmission Electron Microscopy Images Using Machine Learning. *Mathematics* **2021**, *9* (11). https://doi.org/10.3390/math9111209.

(183) Van Den Eeckhout, K.; Bos, A. J. J.; Poelman, D.; Smet, P. F. Revealing Trap Depth Distributions in Persistent Phosphors. *Phys. Rev. B - Condens. Matter Mater. Phys.* **2013**, *87*, 045126.

(184) Van den Eeckhout, K.; Smet, P. F.; Poelman, D. Persistent Luminescence in Eu^{2+}-Doped Compounds: A Review. *Materials* **2010**, *3*, 2536–2566.

(185) Da Silva, M. N.; De Carvalho, J. M.; De Abreu Fantini, M. C.; Chiavacci, L. A.; Bourgaux, C. Nanosized $ZnGa_2O_4$:Cr^{3+} Spinels as Highly Luminescent Materials for Bioimaging. *ACS Appl. Nano Mater.* **2019**, *2*, 6918–6927.

(186) Lin, Y.; Hu, J.; Wu, L.; Zou, Q.; Chen, D.; Huang, D.; Lu, H.; Wang, S. Bin; Zhu, H. Multiple Emission Bands NIR-Persistent Luminescence $mSiO_2$@$Zn_{0.6}Ca_{0.4}Ga_2O_4$:Cr^{3+},Yb^{3+} nanoparticles for Biological Applications. *J. Mater. Chem. B* **2021**, *9*, 1131–1137.

(187) Basavaraju, N.; Sharma, S.; Bessière, A.; Viana, B.; Gourier, D.; Priolkar, K. R. Red Persistent Luminescence in $MgGa_2O_4$:Cr^{3+}; A New Phosphor for in Vivo Imaging. *J. Phys. D. Appl. Phys.* **2013**, *46*, 375401.

(188) Adachi, S. Review—Photoluminescence Properties of Cr^{3+}-Activated Oxide Phosphors. *ECS J. Solid State Sci. Technol.* **2021**, *10*, 026001.

(189) Chen, Z. Z.; Wang, L. C.; Manoharan, D.; Lee, C. L.; Wu, L. C.; Huang, W. T.; Huang, E. Y.; Su, C. H.; Sheu, H. S.; Yeh, C. S. Low Dose of X-Ray-Excited Long-Lasting Luminescent Concave Nanocubes in Highly Passive Targeting Deep-Seated Hepatic Tumors. *Adv. Mater.* **2019**, *31*, 1905087.

(190) Li, Z.; Zhang, Y.; Wu, X.; Wu, X.; Maudgal, R.; Zhang, H.; Han, G. In Vivo Repeatedly Charging Near-Infrared-Emitting Mesoporous SiO_2/$ZnGa_2O_4$:Cr^{3+} Persistent Luminescence Nanocomposites. *Adv. Sci.* **2015**, *2*, 1500001.

(191) Beke, D.; Nardi, M. V.; Bortel, G.; Timpel, M.; Czigány, Z.; Pasquali, L.; Chiappini, A.; Bais, G.; Rudolf, M.; Zalka, D.; Bigi, F.; Rossi, F.; Bencs, L.; Pekker, A.; Márkus, B. G.; Salviati, G.; Saddow, S. E.; Kamarás, K.; Simon, F.; Gali, A. Enhancement of X-Ray-Excited Red Luminescence of Chromium-Doped Zinc Gallate via Ultrasmall Silicon Carbide Nanocrystals. *Chem. Mater.* **2021**, *33*, 2457–2465.

(192) Viana, B.; Sharma, S. K.; Gourier, D.; Maldiney, T.; Teston, E.; Scherman, D.; Richard, C. Long Term in Vivo Imaging with Cr^{3+} Doped Spinel Nanoparticles Exhibiting Persistent Luminescence. *J. Lumin.* **2016**, *170*, 879–887.

(193) Allix, M.; Chenu, S.; Véron, E.; Poumeyrol, T.; Kouadri-Boudjelthia, E. A.; Alahraché, S.; Porcher, F.; Massiot, D.; Fayon, F. Considerable Improvement of Long-Persistent Luminescence in Germanium and Tin Substituted $ZnGa_2O_4$.

Chem. Mater. **2013**, *25*, 1600–1606.

(194) Li, L.; Wang, Y. H.; Li, H.; Huang, H. J.; Zhao, H. Suppression of Photocatalysis and Long-Lasting Luminescence in $ZnGa_2O_4$ by Cr^{3+} Doping. *RSC Adv.* **2015**, *5*, 57193–57200.

(195) Xu, H.; Chen, G. Enhancing near Infrared Persistent Luminescence from Cr^{3+}-Activated Zinc Gallogermanate Powders through Ca^{2+} Doping. *Opt. Mater. Express* **2017**, *7*, 2783–2792.

(196) Maldiney, T.; Lecointre, A.; Viana, B.; Bessière, A.; Bessodes, M.; Gourier, D.; Richard, C.; Scherman, D. Controlling Electron Trap Depth to Enhance Optical Properties of Persistent Luminescence Nanoparticles for in Vivo Imaging. *J. Am. Chem. Soc.* **2011**, *133*, 11810–11815.

(197) Yu, M.; Lin, J.; Zhou, Y. H.; Wang, S. B. Citrate-Gel Synthesis and Luminescent Properties of $ZnGa_2O_4$ Doped with Mn^{2+} and Eu^{3+}. *Mater. Lett.* **2002**, *56*, 1007–1013.

(198) Li, Z.; Zhang, Y.; Wu, X.; Huang, L.; Li, D.; Fan, W.; Han, G. Direct Aqueous-Phase Synthesis of Sub-10 nm “Luminous Pearls” with Enhanced in Vivo Renewable near-Infrared Persistent Luminescence. *J. Am. Chem. Soc.* **2015**, *137*, 5304–5307.

(199) Srivastava, B. B.; Kuang, A.; Mao, Y. Persistent Luminescent Sub-10 nm Cr Doped $ZnGa_2O_4$ Nanoparticles by a Biphasic Synthesis Route. *Chem. Commun.* **2015**, *51*, 7372–7375.

(200) Zhou, Z.; Zheng, W.; Kong, J.; Liu, Y.; Huang, P.; Zhou, S.; Chen, Z.; Shi, J.; Chen, X. Rechargeable and LED-Activated $ZnGa_2O_4$:Cr^{3+} near-Infrared Persistent Luminescence Nanoprobes for Background-Free Biodetection. *Nanoscale* **2017**, *9*, 6846–6853 .

(201) Wei, X.; Huang, X.; Zeng, Y.; Jing, L.; Tang, W.; Li, X.; Ning, H.; Sun, X.; Yi, Y.; Gao, M. Longer and Stronger: Improving Persistent Luminescence in Size-Tuned Zinc Gallate Nanoparticles by Alcohol-Mediated Chromium Doping. *ACS Nano* **2020**, *14*, 12113–12124.

(202) Li, Y. J.; Yang, C. X.; Yan, X. P. Biomimetic Persistent Luminescent Nanoplatform for Autofluorescence-Free Metastasis Tracking and Chemophotodynamic Therapy. *Anal. Chem.* **2018**, *90*, 4188–4195.

(203) Li, Y. J.; Yan, X. P. Synthesis of Functionalized Triple-Doped Zinc Gallogermanate Nanoparticles with Superlong near-Infrared Persistent Luminescence for Long-Term Orally Administrated Bioimaging. *Nanoscale* **2016**, *8*, 14965–14970.

7 GENERAL CONCLUSION

Briefly, materials with UC and PL properties involving NIR illumination (excitation and emission) were successfully developed here.

The lanthanide-doped fluoride-based UCNPs showed high degree of monodispersity, uniform size and mainly spherical shape.

The vital role that different factors have on the morphological, structural, optical, and photoluminescent properties of UCNPs was demonstrated. The content of the activator ions directly determines the color of the light emitted by the UCNPs. It is important to choose the activator ion according to the required applications. For this, it must be considered if the wavelength emitted by them fits the needs. In addition, the adequate concentration can avoid cross-relation processes between the dopant ions. On the contrary, high concentrations can negatively affect emission processes due to non-radiative relaxation processes such as cross-relaxation or energy migration to surface quenching sites.

Particularly high concentrations of Yb^{3+} can induce further growth of nanocrystals. Higher concentrations of Yb^{3+} and larger sizes of the nanoparticles may be suitable for the UC under 980 nm laser excitation, especially when the conversion of three or more photons is required. However, coating of the core nanoparticle with an inactive layer is generally necessary to prevent surface migration to surface quenching sites. Therefore, coating the core nanoparticle with a shell can increase several times the UC luminescence intensity.

Regarding the PLNPs, a relationship was found between the nanoparticle/crystallite size and the PL properties. In addition, it was shown that the synthesis conditions (for example, variation in the type of solvent), influence the growth of the nanoparticles and, consequently, the PL properties.

The main conclusions of each chapter of this thesis are shown below.

First, in Chapter 3, sub-20 nm Nd^{3+}-sensitized Gd^{3+}-based core/shell/shell UCNPs showed simultaneous emission of Tm^{3+} (blue) and Er^{3+} (green and red) ions under 808 nm laser irradiation. The color of the emitted light was thus tuned from blue to white by controlling the concentration of the dopant ions. It was demonstrated that the doping of Tm^{3+} and Er^{3+} ions in the core and outermost shell domains, respectively, as well as the enrichment of the intermediate shell with Nd^{3+}, prevents cross-relaxation processes between them. Furthermore, the precise control of the content and concentration of

the dopant ions in each domain, as well as the thickness of each layer, plays a vital role in the energy transfer process. These results contribute to the development of new materials with multicolor emission and the understanding of energy transfer mechanisms between sensitizer and activator ions. In addition, it helps to understand possible routes to alleviate deleterious processes that decrease the radiative emission *via* quenching the excitation energy.

Chapter 4 addresses and offers solutions to two major problems associated with the use of otherwise very photoactive and promising Ag_3PO_4 photocatalyst: (i) the *lack of photoactivity in the NIR region* and (ii) *limited photostability due to self(photo)reduction involving reduction from* Ag^+ *to* Ag^0. Problem (i) is addressed here by combining Ag_3PO_4 with $NaYbF_4$:Tm^{3+} UCPs. These UCPs showed quite intense UC luminescence in the UV-Vis region under NIR irradiation using a 980 nm laser. The photons emitted by the UCPs have enough energy to photoexcite Ag_3PO_4, thus extending its application to the NIR region. Consequently, the activation of Ag_3PO_4 can occur indirectly with NIR light, in addition to its direct photoexcitation using low-cost commercial LEDs. The problem of limited photostability and poor recyclability of Ag_3PO_4 is addressed here using a minute quantity of hydrogen peroxide (H_2O_2) as the oxidant and photocatalyst regenerating agent that prevents the reduction of Ag^+ and/or assists in the oxidation of Ag^0 back to Ag^+, thus ensuring the structural integrity and recyclability of the photocatalyst. Interestingly, the H_2O_2-induced photocatalyst regeneration process produces reactive oxygen species long after the photoexcitation process has been turned off (light off condition) and thus the photocatalytic system remains active even under dark conditions, leading to the photodegradation of CV dye both under light on and light off conditions. The simple but practical approach introduced in Chapter 4 marks a significant advancement in the development of recyclable photoactive materials for diverse photo(eletrochemical) applications.

UCNPs or UCPs can also be implemented to develop many other systems based on the UC process, for example, they could be combined with ZGO PLNPs to develop NIR rechargeable optical batteries, which may find potential applications in bioimaging and photodynamic therapy. Therefore, the synthesis of ZGO PLNPs and their coupling with UCNPs was also investigated here.

Regarding the obtaining of ZGO PLNPs, Chapter 5 addresses and offers solutions to three fundamental limitations of PL materials: (i) the *lack of precise control over particle size/distribution*, (ii) the *short-lived PL for small nanoparticles*, and (iii) their

poor water dispersibility and/or *limited colloidal stability* required for certain biological applications. *Problem (i)* have been addressed by using a solvothermal synthesis approach employing OA as the nanoparticle stabilizing/capping agent, which prevents their agglomeration and irregular growth. *Problem (ii)* have been addressed by increasing the nanoparticle size in a controlled way using a seed-mediated growth approach, which was accompanied by an increase in PL. *Problem (iii)* have been addressed using surface modification strategies through ligand exchange of the hydrophobic OA molecules, anchored to the nanoparticles surface, by hydrophilic molecules (PAA and Cys, in conjunction with $NOBF_4$), which allows its redispersion in aqueous media and confers long-term colloidal stability. Furthermore, the carboxyl and amino groups anchored to the surface of these nanoparticles are suitable for functionalization with various biomolecules or other types of materials including UCNPs, and thus are relevant for biological applications.

The proposed generalized strategy, which satisfies several prerequisites in relation to bioapplications, could be employed to prepare different kinds of surface-functionalized PLNPs for bioapplications.

Finally, for developing an UC-PL system the coupling of hydrophilic UCNPs and PLNPs was investigated here. An UC-PL system may be able to function as an "optical battery", rechargeable under NIR irradiation and with PL emission also in the NIR region, which makes it attractive for applications requiring deep penetration of the excitation and emission light. The coupling reactions were performed based on EDC/NHS coupling chemistry for the formation of amide groups. The results suggest that the carboxylic and/or amino functional groups anchored to the surface of the nanoparticles are essential for the formation of covalent bonds in the coupling process between them. However, new coupling conditions and the study of resonant energy transfer between UCNPs and PLNPs should be better investigated to ensure possible applications.

8 RESUMO EXPANDIDO DA TESE EM PORTUGUÊS

Esta seção apresenta resumidamente os principais resultados desta tese de doutorado.

Inicialmente, foram obtidas nanopartículas de conversão ascendente de energia (UCNPs) baseadas em Gd^{3+} e sensibilizadas com Nd^{3+} para emissão simultânea dos íons Tm^{3+} (azul) e Er^{3+} (verde e vermelho) sob excitação de 808 nm.

Para obter uma emissão multicolorida eficiente dos UCNPs e evitar relaxações cruzadas deletérias entre os íons Ln^{3+} ativadores (localizados no núcleo e/ou na casca), é essencial obter nanopartículas com nanoestrutura adequada.

A Figura 1a esquematiza um design apropriado para obter emissão multicolorida a partir dos íons Tm^{3+} e Er^{3+} sob excitação em 808 nm dos íons Nd^{3+}.

A separação dos íons ativadores em diferentes camadas (Tm^{3+} no núcleo e Er^{3+} na casca2), juntamente com a dopagem relativamente alta de Nd^{3+} na casca1 permite a transferência de energia de maneira bidirecional, evitando processos de relaxação cruzadas entre esses íons.

A Figura 1b mostra o diagrama ilustrativo da obtenção das nanopartículas com nanoestrutura do tipo núcleo/casca/casca com composição $NaGdF_4$:Yb^{3+}(40)/Ca^{2+}(7)/Nd^{3+}(1)/Tm^{3+}(0,75)@$NaGdF_4$:Nd^{3+}(30)/Ca^{2+}(7)@$NaGdF_4$:Yb^{3+}(40)/Ca^{2+}(7)/Nd^{3+}(1)/Er^{3+}(X = 1, 2, 3, 5, 7 mol%) [doravante referido como CSS (Er^{3+} = 1, 2, 3, 5 e 7)] mediante o crescimento das respectivas nanopartículas núcleo e núcleo/casca (doravante referido como CS).

As imagens de TEM na Figura 1c revelam a formação de nanopartículas esféricas de 7, 12 e 19 nm, respectivamente, para as nanopartículas com estrutura do tipo núcleo (i), CS (ii) e CSS (iii).

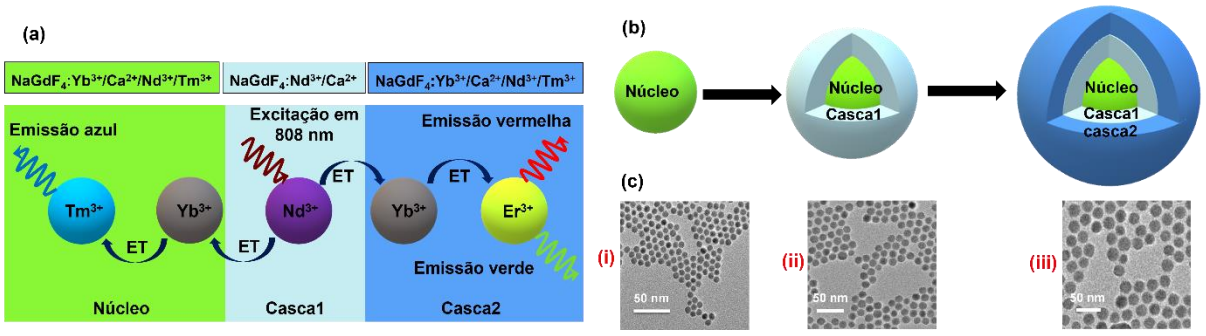

Figura 1 Diagrama esquemático do design do tipo núcleo/casca/casca para emissão multicolorida a partir dos íons Tm^{3+} (no núcleo) e Er^{3+} (na casca2) sob excitação dos íons Nd^{3+} em 808 nm (a). Ilustração esquemática da síntese das UCNPs CSS seguindo um método de crescimento camada por camada mediado por sementes (b). Imagens de microscopia.

Para investigar o efeito das cascas sobre as propriedades óptica foram medidos os espectros de UC das UCNPs de estrutura do tipo núcleo, CS e CSS(Er^{3+} = 5) sintetizadas sob excitação de laser de 808 nm (Figura 2a).

Os picos de luminescência de UC centrados em torno de 451 e 477 nm são atribuídos às transições $^1D_2 \rightarrow {}^3F_4$ e $^1G_4 \rightarrow {}^3H_6$ dos íons Tm^{3+}, respectivamente. A intensidade de luminescência de UC integrada na faixa de 442 a 505 nm é 77 vezes maior após o revestimento da nanopartícula núcleo com a casca. A razão por trás dessa observação pode ser explicada com base em dois fatores. Primeiro, a severa supressão da energia relacionada à superfície das nanopartículas núcleo $NaGdF_4$:Tm^{3+}(0,75)/Yb^{3+}(40)/Nd^{3+}(1)/Ca^{2+}(7) é diminuída pelo revestimento com a camada de $NaGdF_4$:Nd^{3+}(30)/Ca^{2+}(7). Em segundo lugar, a alta concentração de íons Nd^{3+} (30 mol%) na casca das UCNPs CS pode coletar a luz em 808 nm de forma mais eficiente e posteriormente transferi-la para a região central (núcleo) para sensibilizar os íons Yb^{3+} e simultaneamente a Íons Tm^{3+} (ativador) para produzir emissão azul.

Após o crescimento da segunda casca (ou seja, $NaGdF_4$:Yb^{3+}(40)/Nd^{3+}(1)/Ca^{2+}(7)/Er^{3+}(5) na superfície das nanopartículas CS, a luminescência de UC de ambos os ativadores (Er^{3+} e Tm^{3+}) foi observada em conjunto (espectro azul na Figura 2a). Junto com as transições $^1D_2 \rightarrow {}^3F_4$ e $^1G_4 \rightarrow {}^3H_6$ dos íons Tm^{3+}, o pico de emissão verde centrado em 544 nm ($^4S_{3/2} \rightarrow {}^4I_{15/2}$) e o pico de emissão vermelho centrado em 650 nm ($^4F_{9/2} \rightarrow {}^4I_{15/2}$) dos íons Er^{3+} também são observados. Esses resultados comprovam que a casca enriquecida com Nd^{3+} pode coletar a luz de excitação de forma eficiente e permite a migração de energia através da interface núcleo/casca para íons Tm^{3+} no núcleo e Er^{3+} na camada mais externa para produzir luminescência de UC multicolorido a partir das nanopartículas CSS.

O controle preciso da concentração dos íons Er^{3+} na camada mais externa das nanopartículas CSS os torna candidatos potenciais para produzir eficiente luminescência de UC multicolorida. É evidente a partir da Figura 2b que o ajuste apropriado da concentração de Er^{3+} na camada mais externa desempenha um papel essencial na mudança nas intensidades relativas das cores de emissão verde ($^4S_{3/2} \rightarrow {}^4I_{15/2}$) e vermelha ($^4F_{9/2} \rightarrow {}^4I_{15/2}$) dos íons Er^{3+}, resultando na produção de cores luminescência que variam do azul ao branco. Tais mudanças espectrais também podem ser observadas a olho nu como mostrado nas imagens digitais inseridas na Figura 2b.

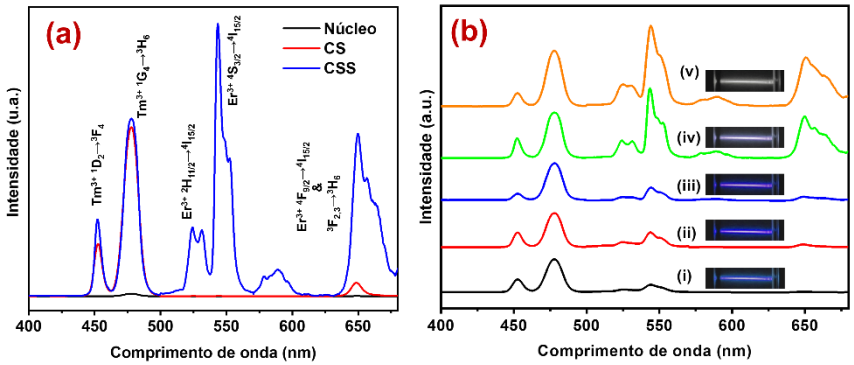

Figura 2 (a) Espectros de luminescência de UC das nanopartículas com estrutura do tipo núcleo, CS (30 mol% de Nd^{3+} na casca) e CSS (5 mol% de Er^{3+} na camada mais externa). (b) Espectros de luminescência de UC das nanopartículas com estrutura CSS com diferentes concentrações de Er^{3+} [(i) = 1, (ii) = 2, (iii) 3, (iv) = 5 e (v) = 7 mol%]. Estão inseridas em (b) às respetivas imagens digitais das correspondentes nanopartículas. Os experimentos foram realizados sob excitação laser de 808 nm.

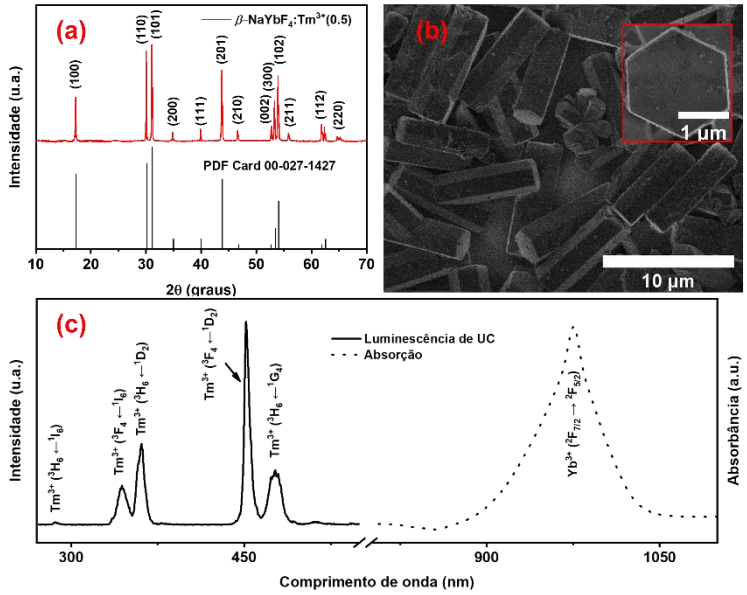

Figura 3 (a) padrão DRX, (b) imagem MEV e (c) espectro de absorção UV-Vis-NIR (linha pontilhada) e espectro de luminescência de UC sob irradiação laser de 980 nm (linha sólida preta) das UCPs de composição $NaYbF_4:Tm^{3+}$. A inserção em (b) mostra uma visão ampliada de uma única partícula orientada verticalmente.

Por outro lado, também foram sintetizadas partículas de conversão ascendente de energia (UCPs) de composição $NaYbF_4:Tm^{3+}$. Estas UCPs foram obtidos pelo tratamento hidrotérmico assistido por micro-ondas, usando ácido etilenodiaminotetracético (EDTA) como agente coprecipitante. Suas propriedades estruturais, morfológicas e ópticas, foram estudadas usando espectroscopia de XRD, SEM e fotoluminescência (PL), respectivamente (Figura 3).

Os padrões de difração de raios-X das UCPs encaixam perfeitamente com o padrão de difração padrão da fase hexagonal dos cristais de β-$NaYbF_4$ (PDF nº 27-

1427) (Figura 3a) que geralmente está associada a luminescência de UC mais forte do que a fase cúbica (α-$NaYbF_4$).

Esta amostra consiste em microbastões de cerca de 7,9 ± 1,4 μm de comprimento e 2,5 ± 0,5 μm de diâmetro (Figura 2b). Uma vista ampliada de um microbastão orientado verticalmente revela a sua forma hexagonal (inserção na Figura 3b), de acordo com os resultados da análise de XRD (Figure 3a).

A presença de íons Yb^{3+} e/ou propriedades de absorção NIR das UCPs são evidentes a partir do pico de absorção característico do Yb^{3+} em cerca de 975 nm no espectro de absorção eletrônico, obtido pela medição da refletância difusa da amostra em pó (Figura 3c, linha pontilhada).

A presença do Yb^{3+} permite assim que as UCPs absorvam os fótons NIR fornecidos pelo laser de 980 nm, enquanto a dopagem com o íon Tm^{3+} como ativador auxilia na obtenção de luminescência de UC na região UV e visível do espectro (Figura 3c , linha contínua).

O espectro de UC das UCPs em suspensão aquosa, medido sob excitação de laser de 980 nm, mostra assim picos de emissão centrados em torno de 286, 344, 361, 452 e 477 nm que são, respectivamente, atribuídos às transições $^1I_6 \rightarrow {}^3H_6$, $^1I_6 \rightarrow {}^3F_4$, $^1D_2 \rightarrow {}^3H_6$, $^1D_2 \rightarrow {}^3F_4$ e $^1G_4 \rightarrow {}^3H_6$ dos íons Tm^{3+} (Figure 3c, linha contínua).

Seguidamente, os microbastões de UC sintetizados foram usados na ativação do Ag_3PO_4, fotocatalisador altamente fotoativo na região UV-Vis, mediante os fótons emitidos sob excitação no NIR. O Ag_3PO_4 foi sintetizado mediante uma metodologia fácil de precipitação usando acetato de prata (CH_3COOAg) e $Na_2HPO_4.12H_2O$ como precursores. Após calcinação a 200 °C, as propriedades morfológicas, composicionais, cristalográficas e ópticas das partículas de Ag_3PO_4 foram estudadas usando SEM, EDX, XRD e DRS, respectivamente. A imagem de SEM do Ag_3PO_4 revela a formação de partículas quase esféricas de tamanho micrométrico (diâmetro médio: 475 ± 182 nm) (Figura 4a). Também se observa que a superfície destas partículas está decorada com pequenas nanoesferas (diâmetro médio aproximado: 16 ± 4 nm) (Figura 4a), que podem corresponder à formação de nanopartículas de Ag na superfície do Ag_3PO_4 calcinado, promovidas pelo tratamento térmico. O espectro de EDS (Figure 4b) mostra claras linhas de emissão de Ag, P e O, confirmando a presença desses elementos nas amostras. O difratograma de XRD na Figure 4c, mostra que todos os picos de difração da amostra encaixam perfeitamente com os da fase cúbica de corpo centrado de Ag_3PO_4 (PDF no. 06-0505).

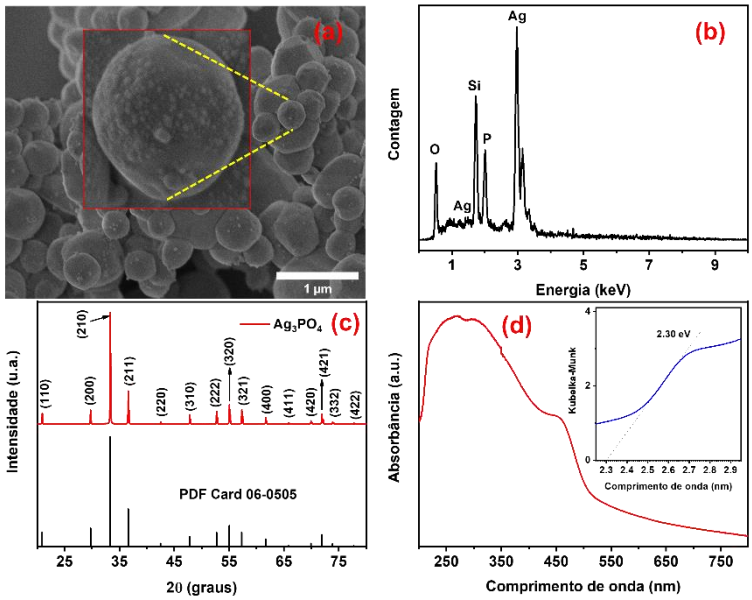

Figure 4 (a) imagem de SEM, (b) espectro de EDS, (c) padrão DRX e (d) espectro de absorção UV-Vis-NIR do fotocatalisador Ag_3PO_4. O sinal do Si no espectro EDS é atribuído ao porta-amostra. A inserção em (a) mostra uma visão ampliada de uma partícula de Ag_3PO_4. A inserção em (c) mostra o valor do band-gap obtido a partir do gráfico da função de Kubelka-Munk contra a energia (eV).

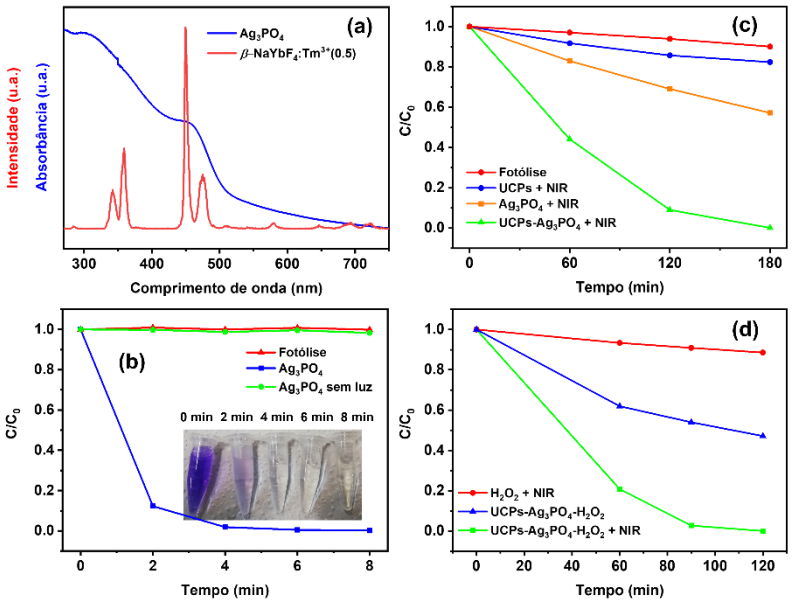

Figura 5 Sobreposição do espectro de absorção do fotocatalisador Ag_3PO_4 com o espectro de luminescência de UC dos microbastões de $NaYbF_4:Tm^{3+}(0,5)$ sob irradiação com laser de 980 nm (a). Mudança temporal na concentração do corante CV em função do tempo de irradiação com LEDs azul (b). Diminuição na concentração do corante CV em função do tempo de irradiação com laser de 980 nm na presença dos sistemas fotocatalíticos UCPs–Ag_3PO_4 (c) e UCPs–Ag_3PO_4–H_2O_2 (d). Além dos experimentos fotocatalíticos na presença de somente Ag_3PO_4 em (b), UCPs-Ag_3PO_4 em (c) e UCPs–Ag_3PO_4–H_2O_2 em (d), diferentes controles também são mostrados.

O espectro de absorção da amostra de Ag_3PO_4 em pó foi medido por espectroscopia de refletância difusa (Figura 4d). Este apresenta forte absorção na

região UV-Vis, atribuída à transferência de carga intrínseca de Ag_3PO_4 da banda de valência (VB) para a banda de condução (CB), com um band-gap indireto de 2,30 eV, como estimado a partir do gráfico de Kubelka-Munk (inserção na Figura 4d).

A forte absorção do Ag_3PO_4 se sobrepõe bem com a emissão de diodos emissores de luz (LEDs) azul (460 ± 10 nm) e com o espectro de emissão dos microbastões de $NaYbF_4:Tm^{3+}$ sob excitação no NIR (Figure 5a), permitindo a fotoexcitação efetiva do Ag_3PO_4 e a fotodegradação de poluentes de maneira direta com os LEDs azul, e de maneira indireta sob irradiação no NIR devido aos fótons emitidos pelas UCPs.

A resposta fotocatalítica do Ag_3PO_4 foi, portanto, avaliada na degradação do corante violeta cristal (CV) sob dois modos de iluminação diferentes, a saber, iluminação com LEDs azul (fotoexcitação direta do Ag_3PO_4) (Figura 5b) e irradiação laser de 980 nm (fotoexcitação indireta de Ag_3PO_4 pelos fótons UV-visível emitidos pelas UCPs) (Figura 5c).

A absorbância normalizada do corante exibiu uma diminuição drástica em apenas 2 min de iluminação com os LEDs (Figure 5b, linha vermelha) e quase 100% de descoloração do corante foi alcançado em menos de 8 min (veja a inserção na Figura 5b), indicando a alta atividade fotocatalítica sob luz visível das partículas de Ag_3PO_4 preparadas.

Depois de confirmar a excelente atividade fotocatalítica inerente do Ag_3PO_4 sob luz visível foi avaliada a fotoatividade no NIR do sistema composto pelas UCPs e o fotocatalisador (UCPs-Ag_3PO_4) (Figura 5c). Foi observada uma degradação de quase 100% do corante em 180 min sob na presença do sistema UCPs-Ag_3PO_4 sob irradiação laser (Figura 5c), confirmando, portanto, sua fotoatividade baseada no NIR. Além disso, a presença de H_2O_2 levou a uma melhora considerável na degradação do corante sob irradiação de laser de 980 nm, atingindo quase 100% de degradação do corante em apenas 90 min de iluminação no NIR (Figura 5d).

Experimentos controle foram realizados para entender melhor o processo fotocatalítico e avaliar a contribuição de diferentes fatores. Por exemplo, pode-se notar que a diminuição da absorbância do corante no experimento de adsorção (Ag_3PO_4 sem luz) (Figura 5b, linha verde) e a fotólise direta do corante sob irradiação com luz visível (Figura 5b, linha vermelha) e com laser de 980 nm, independentemente da ausência (Figura 5c, linha vermelha) ou presença de H_2O_2 (Figuras 5 d, linha vermelha), é insignificante.

Da mesma forma, observamos uma diminuição de cerca de 40% na concentração do corante CV na presença de apenas Ag_3PO_4 (linha laranja na Figura 5c) sob irradiação laser de 980 nm. Isso pode ser atribuído à excitação direta no NIR do Ag_3PO_4 altamente fotoativo.

De maneira similar, foi observada uma redução significativa na concentração do corante CV pelo sistema UCPs-Ag_3PO_4-H_2O_2 na ausência de iluminação NIR (linha azul na Figura 5d), o que pode ser associado à produção de espécies reativas de oxigênio, mediante reação do tipo Fenton entre H_2O_2 e as partículas de Ag na superfície de Ag_3PO_4 formadas durante o processo de calcinação. Em todos os casos, a diminuição da concentração do corante CV na presença do sistema UCPs–Ag_3PO_4 e/ou UCPs–Ag_3PO_4–H_2O_2 sob irradiação com laser de 980 é muito maior (~100%), confirmando a atividade fotocatalítica baseada no NIR desses dois sistemas.

Além do uso na fotocatálise heterogênea, os materiais com propriedades de UC também podem ser empregados na excitação de outros materiais, por exemplo, PLNPs. As características resultantes da combinação de UCNPs com PLNPs podem oferecer desvantagens proeminentes para bioaplicações. As PLNPs possuem a capacidade única de funcionar como baterias ópticas (ou seja, armazenar energia de excitação) e emitir fótons de energia mais baixa por um longo tempo após desligar a luz de excitação externa. Isso permite uma diminuição no tempo de exposição do tecido à radiação de excitação e, adicionalmente, à diminuição do sinal de fundo de autofluorescência em comparação com o uso particular das UCNPs.

Em particular o galato de zinco dopado com crômio ($ZnGa_2O_4:Cr^{3+}$, doravante nomeado como ZGO) apresenta luminescência persistente no NIR entorno de 700 nm. Da mesma forma que a radiação de excitação das UCNPs em 980 nm a emissão do ZGO encontra-se na primeira janela biológica, ou seja, em uma região de baixa absorção pelos tecidos biológicos, aumentando notavelmente a profundidade de detecção e melhora da eficácia terapêutica.

Devido ao mencionado anteriormente, neste trabalho também foram sintetizadas PLNPs de ZGO para posteriormente investigar o acoplamento com UCNPs.

As PLNPs de ZGO foram sintetizados mediante um método solvotérmico líquido–sólido–solução de acordo com metodologias adaptadas da literatura. Usou-se uma mistura de OA, NaOH, álcoois de cadeia curta, água e os nitratos de Zn^{2+}, Ga^{3+} e Cr^{3+}. Estas amostras revestidas com OA exibiram algumas mudanças em sua morfologia, tamanho de partícula, tamanho de cristalito, bem como nas suas propriedades

luminescentes, dependendo do tipo de álcool usado na síntese (Figure 6). Os PLNPs sintetizados na presença de propanol (ZGOP, Figura 6a) e etanol (ZGOE, Figura 6b) apresentaram uma morfologia quase esférica e uma distribuição de tamanho unimodal, com diâmetro médio de partícula de 7,1 e 7,7 nm, respectivamente. Por outro lado, a amostra preparada com metanol (ZGOM, Figura 6c) apresentou uma distribuição bimodal com a coexistência de nanopartículas pequenas (10,6 nm) e grandes (64,4 nm), de formato esferoidal e triangular, respectivamente.

A análise de XRD em pó na Figura 6d mostra que todas as amostras de ZGO cristalizaram na fase cúbica do $ZnGa_2O_4$ (PDF Card 00-038-1240), sem a presença de quaisquer impurezas de fase. Os tamanhos de cristalitos obtidos a partir dos difratogramas da Figura 6d, usando a equação de Scherrer são 6,9, 7,2 e 14,2 nm para ZGOP, ZGOE e ZGOM, respectivamente, de acordo com os tamanhos de partículas calculados a partir das imagens TEM correspondentes (Figura 6a-c).

A Figura 6 e-g mostra os espectros de excitação (e) e emissão (f), bem como os decaimentos da luminescência pós-excitação correspondentes à emissão em 697 nm (g). Os decaimentos da luminescência em (g) foram obtidos após excitação das amostras sintetizadas na presença dos três álcoois diferentes durante 2 min com um LED branco e um atraso de 20 segundos. Como pode ser observado a partir dos espectros de excitação (Figura 6e), as amostras apresentam três bandas características, localizadas nas regiões UV (250–350 nm), azul (420 nm) e laranja (540 nm). As bandas localizadas em torno de 420 nm e 540 nm são atribuídas às transições permitidas por spin do estado fundamental [$^4A_2$ (4F)] dos íons Cr^{3+} em uma simetria octaédrica para os estados excitados $^4T_1$ (^4F) e $^4T_2$ (^4F), respectivamente. A outra banda na região UV resulta de uma sobreposição parcial do band gap da matriz hospedeira de $ZnGa_2O_4$ com a transição permitida por spin do estado fundamental [$^4A_2$ (^4F)] para o estado excitado [$^4T_1$ (^4P)] de Cr^{3+} íons. Todas as amostras exibiram um perfil de decaimento semelhante (Figure 6g), que foi ajustado em uma função de decaimento biexponencial (ExpDec2 Fit), indicando dois tempos de vida diferentes e sugerindo que existem pelo menos dois caminhos para a recombinação radiativa dos portadores de carga na produção de luminescência persistente dessas nanopartículas.

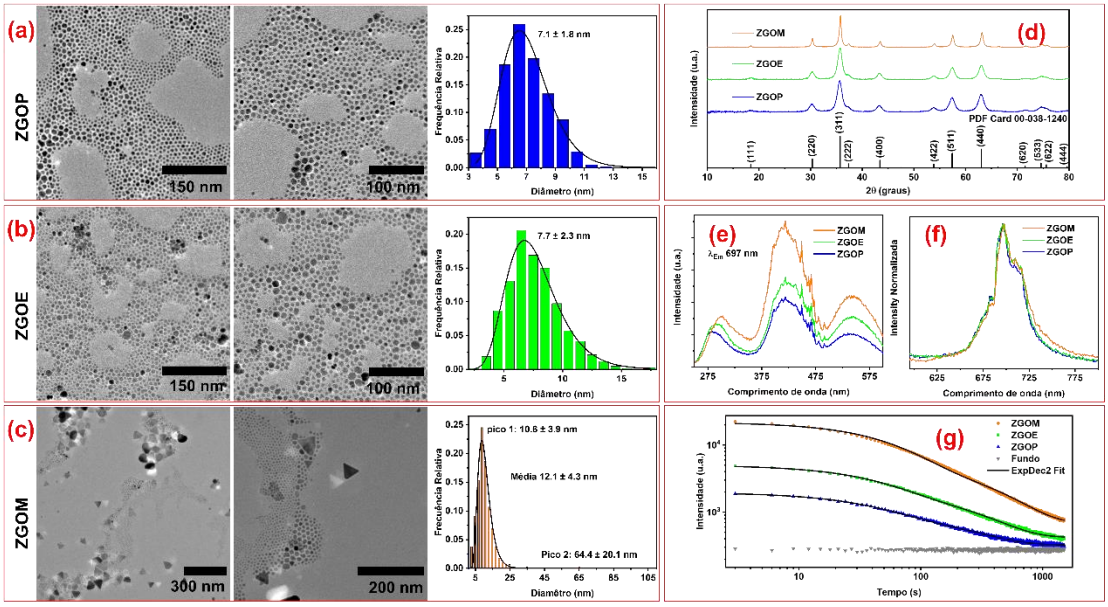

Figura 6 Imagens de TEM em duas ampliações diferentes e a correspondente distribuição de tamanho extraída das imagens de TEM (a-c) das amostras de ZGO preparadas na presença de propanol (a), etanol (b) e metanol (c). XRD (d), espectros de excitação (λ_{em} = 697 nm) (e), espectros de emissão (λ_{exc} = 291 nm) (f) e curva de decaimento de luminescência pós-excitação (g) das correspondentes amostras em pó.

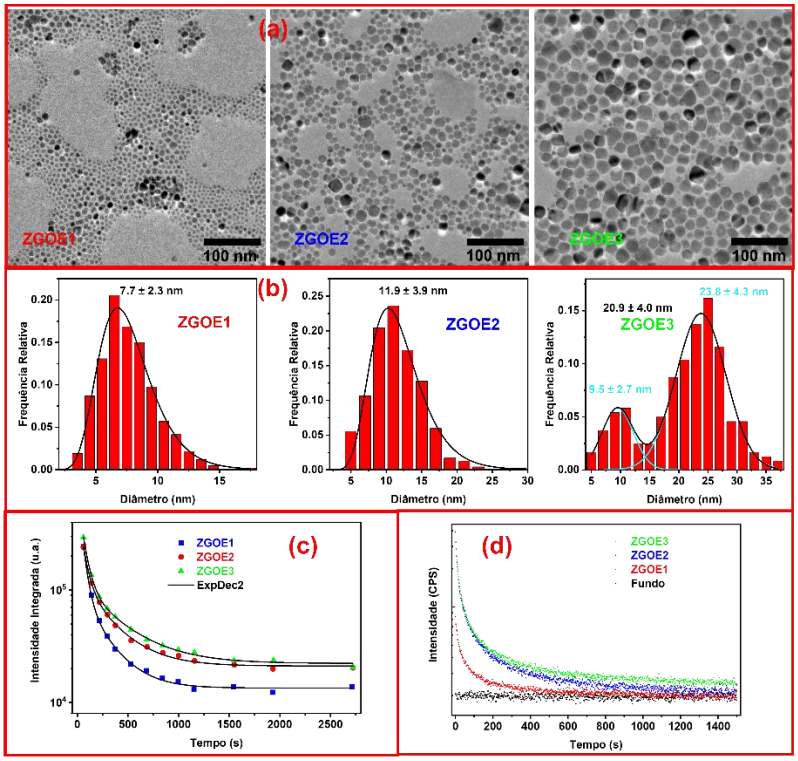

Figura 7 Imagens de TEM (a), distribuição de tamanho calculada a partir das correspondentes imagens de TEM (b) e curvas de decaimento da luminescência persistente (c e d) das mostras de ZGO com diferentes tamanhos. As curvas em (c) foram obtidas a partir do cálculo das intensidades integradas dos espectros de emissão (601–790 nm) em diferentes intervalos de tempo pós-excitação (λ_{exc} = 291 nm). As curvas em (d) correspondem ao decaimento da emissão (λ_{em} = 697 nm) pós-excitação (LED branco). A excitação das amostras realizou-se durante 120 s; atraso pós-irradiação de 25 e 5 s para (c) e (d), respectivamente. Todos os experimentos foram realizados em ciclohexano.

Para preparar partículas ligeiramente maiores com propriedades de luminescência aprimoradas, foram empregadas as pequenas nanopartículas ZGOE (7,7 nm) (agora denominadas ZGOE1) como sementes para sintetizar nanopartículas maiores (ZGOE2) de aproximadamente 12 nm (veja Figura 7 a,b). Subsequentemente, as ZGOE2 resultantes foram usadas como sementes para preparar nanopartículas ainda maiores (ZGOE3) (veja Figura 7 a,b). No entanto, a amostra ZGOE3 mostrou uma distribuição de tamanho bimodal (9,5 nm e 24 nm), sugerindo que o crescimento do cristal é acompanhado por nucleação fresca.

Seguidamente, as amostras dispersadas em ciclohexano foram irradiadas a 291 nm (λ_{exc}) durante 120 s. Os espectros de luminescência (601–790 nm) pós-excitação começaram ser registrados 25 s após desligar a luz de excitação. Em seguida, foram calculadas as intensidades integradas (Figura 7c) obtidas a partir desses espectros em diferentes intervalos de tempo pós-excitação. À medida que o tamanho médio de partícula aumentou de 8 para 21 nm, os tempos de vida (t) do primeiro (t_1) e segundo decaimento (t_2) (ajuste ExpDec2) aumentaram de 45 para 56 s e de 233 a 375 s, respectivamente. Esses resultados demonstram o impacto positivo do aumento do tamanho das partículas, via crescimento mediado por sementes, nas propriedades luminescentes das PLNPs.

Da mesma forma, as amostras em ciclohexano foram irradiadas com um LED branco durante 120 s. As curvas de decaimento de luminescência pós-excitação (λ_{em} 697 nm) foram registradas 5 s depois de remover a excitação (Figura 7d). A partir da Figura 7d pode-se inferir que o aumento no tamanho das nanopartículas permite maior armazenamento da energia de excitação. Adicionalmente, as amostras ZGOE3 e ZGOE2 continuaram emitindo fotoluminescência por mais tempo em comparação com ZGOE1, o que novamente apoia a importância de aumentar o tamanho das nanopartículas pelo crescimento mediado por sementes para melhorar as propriedades ópticas das PLNPs de ZGO.

Depois de aprimorar as propriedades de PL das nanopartículas de ZGO revestidas com OA foi realizada a modificação de superfície para remover os ligantes hidrofóbicos e fornecer grupos hidrofílicos na sua superfície. As nanopartículas ZGOE3 foram revestidos com ácido poliacrílico (PAA) mediante uma estratégia de troca de ligante de uma etapa (direta) (rota 1, Figura 8a) e através de uma estratégia de troca de ligante de duas etapas (rota ii, Figura 8a). Neste último caso, as moléculas de OA originais são substituídas por íons BF_4^- usando $NOBF_4$ em N,N-

dimetilformamida (DMF). Posteriormente, os íons BF_4^- são também substituídos pelo polímero PAA em pH 9 (rota ii-a) ou moléculas de cisteamina (rota ii-b). As amostras foram nomeadas como ZGOE3-PAA, ZGOE3-B, ZGOE3-B-PAA e ZGOE3-B-Cys após as modificações de superfície com PAA (rota i), $NOBF_4$ (rota ii), $NOBF_4$/PAA (rota ii-a) , e $NOBF_4$/Cys (rota ii-b), respectivamente.

As imagens de TEM na Figura 8b-e mostram que as nanopartículas ZGOE3 mantiveram seu formato após a modificação da superfície com os diferentes ligantes. Conforme mostrado na Figura 8b, grandes aglomerados de nanopartículas foram obtidos após a modificação de superfície com apenas PAA (ZGOE3-PAA) através da estratégia de uma etapa (rota i). Entretanto, todas as outras modificações de superfície permitiram uma boa dispersão das nanopartículas (Figura 8c-e).

Adicionalmente, as modificações de superfície em duas etapas envolvendo BF_4^- conferiram estabilidade coloidal de longo prazo às nanopartículas em meio aquoso (60 dias ou mais), como evidenciado na Figura 8f (i e ii).

As medições de espalhamento dinâmico de luz (DLS) (Figura 8f) das dispersões aquosas após 60 dias de armazenadas em repouso (sem agitação e após agitação) não mostraram alterações importantes no diâmetro hidrodinâmico das amostras ZGOE3-B-Cys (i) e ZGOE3-B-PAA (ii), em relação ao DLS inicial (antes do período de 60 dias), demonstrando sua boa estabilidade coloidal. A alta estabilidade destas amostras está relacionada ao seu alto valor de potencial ζ (-46 e +40 mV, para ZGOE3-B-PAA e ZGOE3-B-Cys, respectivamente) (Figure 8g).

Por outro lado, a amostra ZGOE3-PAA exibiu um valor de potencial ζ mais baixo (-11 mV, implicando estabilidade coloidal limitada) (Figura 8g) e, portanto, uma distribuição de tamanho hidrodinâmico multimodal [Figura 8f (iii)]. Para esta amostra, os diâmetros hidrodinâmicos bimodais mudam significativamente quando a amostra preparada (184 e 462 nm) é armazenada por 60 dias sem agitação (95 e 408 nm), confirmando que de fato esta amostra tem pobre estabilidade coloidal.

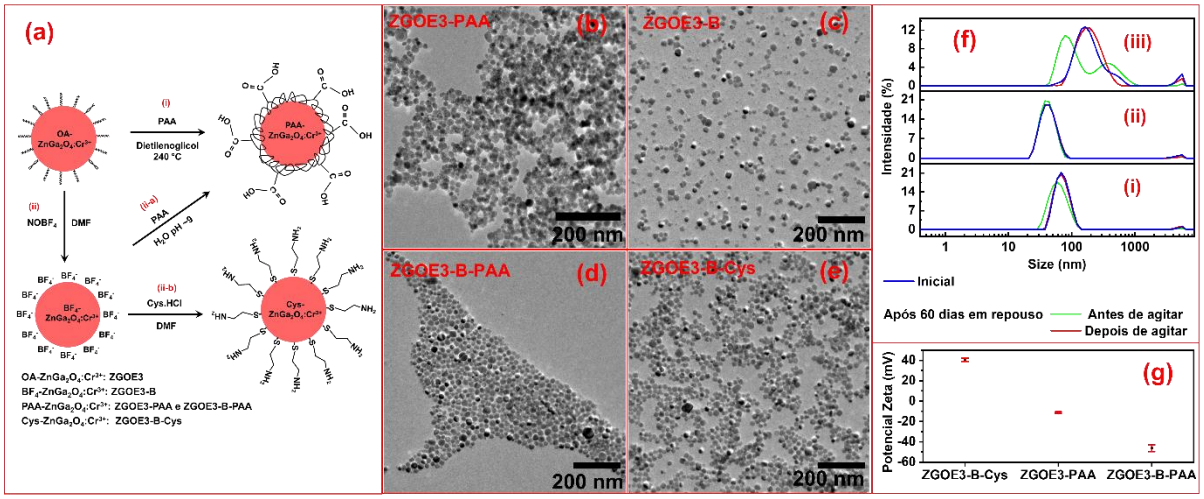

Figura 8 Diagrama esquemático da modificação da superfície das nanopartículas de ZGO através de diferentes estratégias (a). Imagens de TEM ZGOE3 antes e depois das modificações de superfície (b-e). Tamanho hidrodinâmico das amostras antes e após 60 dias em repouso sem agitação e após agitação (f). Valor de potencial ζ das amostras ZGOE3-B-Cys, ZGOE3-PAA e ZGOE3-B-PAA.

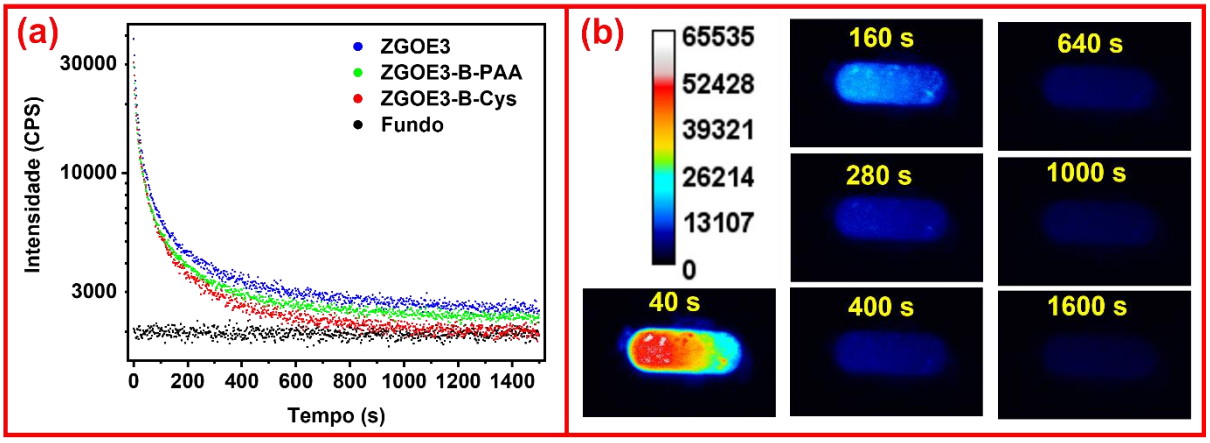

Figura 9 Curvas de decaimento pós-excitação de ZGOE3 (em ciclohexano), ZGOE3-B-PAA (em tampão pH 9) e ZGOE3-B-Cys (em água) (a). Imagens de luminescência da amostra ZGOE3-B-Cys em pó registradas em diferentes intervalos pós-excitação (b). Excitação: 120 s com LED branco; atraso pós-irradiação de 5 s. As imagens de luminescência em (b) contra um fundo preto são representadas com cores falsas onde a cor indica a escala de intensidade de luminescência de preto a branco.

Seguidamente, as curvas de decaimento de luminescência de ZGOE3-B-Cys e ZGOE3-B-PAA foram medidas (Figura 9a) da mesma maneira descrita acima para as amostras revestidos com OA.

As PLNPs hidrofílicos retêm a PL em meio aquoso, e observa-se apenas uma pequena diminuição em sua duração, o que pode estar relacionado à diferença de solvente/meio ou do agente de revestimento das nanopartículas. De fato, as moléculas de Cys são menores e, provavelmente, não fornecem às nanopartículas a mesma proteção que as moléculas maiores de OA ou PAA contra interações com o

solvente, causando dissipação de energia na superfície por interações com grupos O–H de moléculas de água.

Por outro lado, após irradiação da amostra ZGOE3-B-Cys em pó durante 120 s com o LED branco seguiu-se o decaimento da intensidade de luminescência pós-excitação a partir das imagens de luminescência (Figura 9b). Essas imagens mostram a possibilidade de detecção acima de 1500 s, o que é interessante para obtenção de bioimagens de luminescência com baixo sinal de autofluorescência.

Uma vez que se conseguiu boa luminescência persistente e estabilidade coloidal de longo prazo das nanopartículas de ZGO em meio aquoso, o seguinte passo foi a investigação do acoplamento dessas nanopartículas com os materiais com propriedades de UC. Entretanto, as UCPs de $NaYbF_4:Tm^{3+}$ sintetizados anteriormente, que apresentaram forte sinal de luminescência de UC na região UV-Vis, não apresentam um tamanho adequado para esse objetivo.

Por isso procedeu-se sintetizar nanopartículas com estrutura do tipo núcleo/casca e composição $NaYbF_4:Tm^{3+}@NaYF_4$. A emissão UV-Vis foi aprimorada mediante o controle da espessura da casca. Para controlar adequadamente a espessura dessa camada injetou-se diferentes quantidades de pequenas nanopartículas de $NaYF_4$, denominadas *sacrificial nanoparticles* (SNPs), diretamente na mistura de reação das UCNPs centrais (núcleo) de $NaYbF_4:Tm^{3+}$ a 300 °C (veja Figura 10a). As UCNPs de $NaYbF_4:Tm^{3+}$ de aproximadamente 27,2 nm (veja as Figuras 10c) são favorecidas sobre as SNPs de $NaYF_4$ energeticamente menos estáveis de aproximadamente 9,5 nm (veja as Figuras 10b), resultando no crescimento de partículas maiores ($NaYbF_4:Tm^{3+}@NaYF_4$) às custas das menores ($NaYF_4$), formando a estrutura núcleo/casca de $NaYbF_4:Tm^{3+}@NaYF_4$ com diferentes espessuras da casca, desde 1,4 até 3,4 nm, como mostrado na Figura 10 d-g.

Pode-se observar na Figura 11 que o aumento da espessura da casca teve uma influência positiva na intensidade de luminescência de UC medida sob excitação laser de 980 nm. A explicação para esta observação reside no fato de que o revestimento das nanopartículas centrais (núcleo) com uma casca cada vez maior permite uma concomitante redução da dissipação da energia por migração para a superfície, devido à maior distância núcleo-superfície.

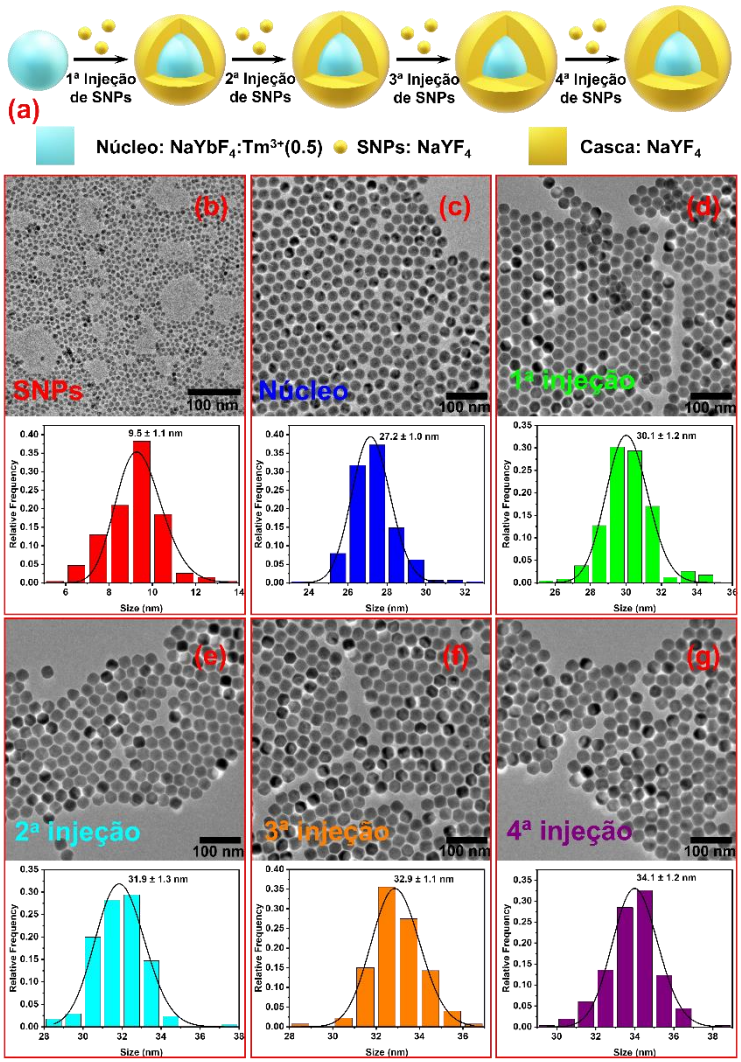

Figura 10 Diagrama esquemático do crescimento da casca a partir das UCNPs de apenas núcleo com injeção de SNPs com base no processo de amadurecimento de Oswald (a). Imagens de TEM e as correspondentes distribuições de tamanho (b-g) das SNPs (b) e as UCNPs de apenas núcleo (c) e de estrutura núcleo/casca com diferentes espessuras da camada de acordo com o número de injeções de SNPs.

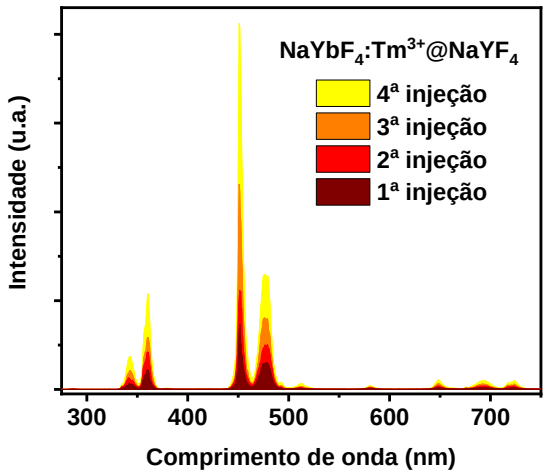

Figura 11 Espectros de luminescência de UC das amostras núcleo/casca de $NaYbF_4:Tm^{3+}@NaYF_4$ com diferentes espessuras de casca. Os espectros foram obtidos sob irradiação com laser de 980 nm.

Após a troca dos ligantes hidrofóbicos por PAA, como foi descrito acima para as PLNPs, procedeu-se com as reações de acoplamento entre as PLNPs e as UCNPs hidrofílicas, usando as nanopartículas com as propriedades ópticas aprimoradas.

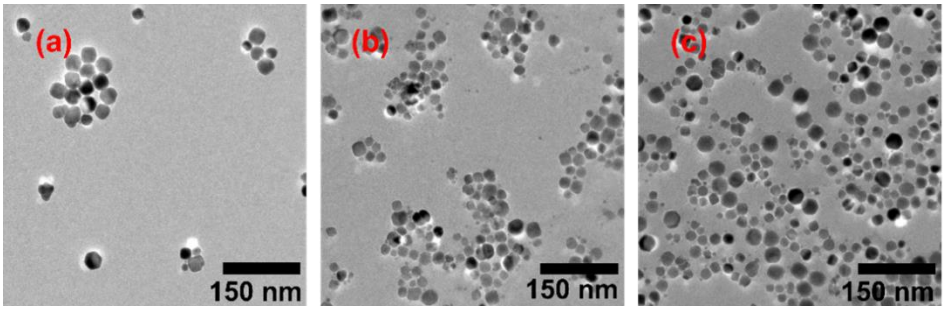

Figura 12 (a-c) Imagens de TEM das nanopartículas produtos das reações de acoplamento dos experimentos (a), (b) e (c), respetivamente, com base na química de acoplamento EDC/NHS em tampão borato pH = 9.

As imagens de TEM na Figura 12, são os resultados do acoplamento entre as PLNPs e as UCNPs com base na química de acoplamento EDC/NHS para a formação de grupo amida. Para o acoplamento entre as nanopartículas revestidas com PAA usou-se o polímero poli(etilenoglicol)bis(amina) (NPEGN), em conjunto com os reagentes EDC e NHS.

Em todos os casos, a quantidade de UCNPs foi fixa, enquanto a quantidade de PLNPs e NPEGN utilizadas foram variadas (ver Tabela 1).

As imagens de TEM sugerem que para a quantidade de PLNPs no experimento da Figura 12a pode ser muito baixa em relação à quantidade de UCNPs, enquanto no experimento da Figura 12c a quantidade de PLNPs em relação à quantidade de UCNPs parece ser adequada. No entanto, ao comparar as Figuras 12 b e c, pode-se observar que a mesma quantidade de NPEGN (0,003 mmol) leva à formação de alguns aglomerados no experimento da Figura 12b (que podem ser devido à formação de ligações covalentes entre os UCNPs e PLNPs), mas não no experimento da Figura 12c. É provável que para o experimento da Figura 12c a quantidade de PLNPs usada (metade do que no experimento da Figura 12b) seja baixa o suficiente para permitir que a quantidade de NPEGN seja ligada a todos os grupos carboxílicos disponíveis na superfície das UCNPs e PLNPs, portanto, o acoplamento entre essas nanopartículas não ocorre ou pode ocorre em menor proporção. Enquanto isso, no experimento da Figura 12b a quantidade de PLNPs pode ser grande o suficiente para que mais grupos carboxílicos estejam disponíveis do que grupos amino do polímero

NPEGN. Consequentemente, alguns grupos carboxílicos estão livres para a reação de acoplamento.

Além disso, é possível observar nanopartículas individuais, inclusive na Figura 12b, o que pode indicar que nem todas as nanopartículas foram ligadas ao realizar esta estratégia de acoplamento.

Por fim, como perspectivas futuras para melhor entendimento desse processo e obtenção de sistemas UC-PL, novos experimentos de acoplamento, assim como caracterizações, incluindo o estudo da transferência de energia entre as nanopartículas será necessário.

Tabela 1 Condições experimentais das reações de acoplamento entre UCNPs e PLNPs.

Experimento de acoplamento	(a)	(b)	(c)
mmol das UCNPs revestidas com PAA	0.025		
mmol das PLNPs revestidas com PAA	0.02	0.1	0.05
mmol de EDC	0.1	0.15	
mmol de NHS	0.04	0.08	
mmol de NPEGN	0.001	0.003	
Médio	Tampão borato pH 9		